DOT/FAA/TC-13/40

Federal Aviation Administration
William J. Hughes Technical Center
Aviation Research Division
Atlantic City International Airport
New Jersey 08405

Three-Dimensional Assisted Defect Recognition Technique for Ultrasonic Inspection

September 2017

Final Report

U.S. Department of Transportation
Federal Aviation Administration

NOTICE

This report is available at the Federal Aviation Administration William J. Hughes Technical Center's Full-Text Technical Reports page: actlibrary.tc.faa.gov in Adobe Acrobat portable document format (PDF).

Technical Report Documentation Page

1. Report No.	2. Government Accession No.	3. Recipient's Catalog No.
DOT/FAA/TC-13/40		

4. Title and Subtitle	5. Report Date
THREE-DIMENSIONAL ASSISTED DEFECT RECOGNITION TECHNIQUE FOR ULTRASONIC INSPECTION	September 2017
	6. Performing Organization Code

7. Author(s)	8. Performing Organization Report No.
Patrick Howard and Andrew Ferro	

9. Performing Organization Name and Address	10. Work Unit No. (TRAIS)
GE Aviation 1 Neumann Way Cincinnati, OH 45215	11. Contract or Grant No. DFACT-10-C-0029

12. Sponsoring Agency Name and Address	13. Type of Report and Period Covered
U.S. Department of Transportation Federal Aviation Administration New England Region—Aircraft Certification Service Engine & Propeller Directorate FAA New England Regional Office 16 New England Executive Park Burlington, MA 01803	14. Sponsoring Agency Code ANE-100

15. Supplementary Notes

The FAA William J. Hughes Technical Center Aviation Research Division CORs were Cu Nguyen and Dave Galella.

16. Abstract

The purpose of this program was to investigate the potential advantages for detection of material anomalies by using three-dimensional (3D) ultrasonic data instead of the traditional two-dimensional (2D) C-scan images. Toward that end, a set of test specimens of different aerospace alloys with real and artificial anomalies was identified. Ultrasonic waveform data were collected on those test specimens to create a set of test images with a broad cross-section of signal-to-noise ratio. Using the set of test images, an assisted defect recognition (ADR) algorithm prototype was developed that used the 3D ultrasonic data. This algorithm was tested extensively, using the broad cross-section of images, and compared to the results of the state-of-the-art 2D ADR techniques. This testing showed three clear advantages of using 3D ADR. First, the 3D algorithm demonstrated improved detection of the material anomalies when compared to the 2D algorithm. Second, 3D ADR reduced false positive (FP) inspection results due to titanium (Ti) microstructure. The FPs increase the cost of ultrasonic inspection by causing the unnecessary scrapping of good material. The third advantage of 3D ADR was that larger volumes of material could be inspected while maintaining the same sensitivity as 2D ADR. This advantage could result in a productivity improvement for the inspection of aerospace billet and forgings. Finally, a demonstration of the 3D ADR technology was held in a production-representative environment for ultrasonic inspection of aerospace forgings. Using a commercial off-the-shelf 3D ultrasonic data acquisition system from OKOS Systems, a small Ti forging with synthetic targets was scanned by an NAS 401 certified level II operator. Full 3D ultrasonic data were collected at over 20″ per second surface speed. The speed was limited to 20″ per second by the performance of the mechanical system. Surprisingly, the ultrasonic data acquisition system did not limit the data acquisition speed and could support higher speeds than demonstrated. The data were analyzed by the level II operator, using the 3D ADR industrial software. The 3D algorithm demonstrated the improved results over the 2D algorithm in this production-representative environment.

17. Key Words	18. Distribution Statement
Ultrasound, Nondestructive testing, Nondestructive evaluation, Image processing, Assisted defect recognition	This document is available to the U.S. public through the National Technical Information Service (NTIS), Springfield, Virginia 22161. This document is also available from the Federal Aviation Administration William J. Hughes Technical Center at actlibrary.tc.faa.gov.

19. Security Classif. (of this report)	20. Security Classif. (of this page)	21. No. of Pages	22. Price
Unclassified	Unclassified	63	

ACKNOWLEDGEMENTS

The authors wish to acknowledge the following individuals for their valuable contributions to the program documented in this report:

- John Friedl and Chester Pawlowski for designing and executing the technical plan for the production demonstration;
- Rich Klaassen, Ed Nieters, and Krzysztof Lesnicki for collecting the ultrasonic data to validate the assisted defect recognition (ADR) system;
- Evan Herberth and Josh Falter for the design and coding of the ADR software for the production demonstration;
- Geoff Shotts of OKOS Systems for technical assistance with the production demonstration;
- The members of the technical working group for providing valuable peer review and feedback on the plans and results for this program;
- and Jon Bartos and Cu Ngyuen for supporting the vision of three-dimensional ultrasonic ADR.

TABLE OF CONTENTS

LIST OF FIGURES

LIST OF TABLES

LIST OF SYMBOLS AND ACRONYMS

Ti	Titanium
2D	Two-dimensional
3D	Three-dimensional
4GL	Fourth-generation language
ADR	Assisted defect recognition
ASIC	Application-specific integrated circuit
ASTM	American Society for Testing and Materials
AUC	Area under the curve
CPU	Central processing unit
DICOM	Digital Imaging and Communications in Medicine
DICONDE	Digital Imaging and Communication in Nondestructive Evaluation
DLL	Direct Link Library
DOE	Design of experiments
FAA	Federal Aviation Administration
FBH	Flat bottom hole
FIR	Finite Impulse Response
FMZ	Forging multizone
FN	False negative
FP	False positive
FPGA	Field-programmable gate array
FROC	Free-response receiver operating characteristic
FPR	False positive rate
GE®	General Electric
GPU	Graphics processing units
HDL	Hardware description language
IDL	Interactive Data Language
IIR	Infinite Impulse Response
NDE	Nondestructive evaluation
NDT	Nondestructive testing
NIH	National Institute of Health
OEM	Original equipment manufacturer
PC	Personal computer
POD	Probability of detection
QTC	GE Aviation Quality Technology Center
RF	Radio frequency
SHA	Synthetic hard alpha
SID	Synthetic inclusion disk
SNR	Signal-to-noise ratio
RF	Radio frequency
ROC	Receiver operating characteristic
ROI	Region of interest
TIFF	Tagged image file format
TN	True negative
TP	True positive

TPR	True positive rate
TWG	Technical working group
UT	Ultrasonic testing

EXECUTIVE SUMMARY

Studies have shown that ultrasonic testing (UT) results, like many nondestructive testing (NDT) methods, are dependent on operator interpretation of the inspection results. In an effort to minimize the variability introduced by operator interpretation, image processing technology has been applied to NDT results. Inspections incorporating this technology are referred to as either automated defect recognition assisted defect recognition (ADR), depending on the level to which the operators are involved in the process. The ADR algorithms applied to industrial UT inspection use only the data available in two-dimensional (2D) C-scans to detect indications. This approach has proven to have a high probability of detection (POD), but false positives (FP) can result because acceptable, but highly reflective, grains in acceptable metallic microstructures cannot be correctly classified any differently from voids or inclusions based on 2D data alone. Because of limitations in computing power and data storage, commonly used industrial UT inspection systems have traditionally been limited to stop-on-defect or C-scan data acquisition. With the improvements in computational power and data storage within the computer industry, the next generation of UT inspection equipment should have the capability to analyze and archive three-dimensional (3D) A-scan data in production environments. This evolution from 2D to 3D ultrasonic data will provide more information for both improvements in detection and the proper classification of material anomalies.

This program focused on the feasibility of using 3D ultrasonic data by extending successful 2D ADR concepts to 3D ultrasonic data sets and demonstrating the potential benefits to the industry in terms of increased detection of melt-related defects and a reduction in FP indications from acceptable microstructures. This research is timely for the industry for several reasons. With the increase in fuel costs, new engine designs will need to provide improved fuel efficiency. Increasing the POD for melt-related defects will enable the engineering teams to consider more fuel-efficient designs. With the recent increases in raw material cost in the aviation industry, reducing the number of FP indications has the potential to significantly impact manufacturing cost. Also, a large portion of the current UT equipment in the industry is 10 to 15 years old and nearing the end of its usefulness. Providing the industry with demonstrations of improvements in both cost savings and inspection quality, 3D UT data analysis techniques have the potential to provide the industry with sufficient substantiation to justify planned reinvestments in new equipment that can take advantage of the increased data analysis methods that ADR provides.

The purpose of this program was to investigate the potential advantages for detection of material anomalies by using 3D ultrasonic data instead of the traditional 2D C-scan images. A set of test specimens of different aerospace alloys with real and artificial anomalies was defined. Ultrasonic waveform data were collected on those test specimens to create a set of test images with a broad cross-section of signal-to-noise ratio.

Using the set of test images, an ADR algorithm prototype was developed that used the 3D ultrasonic data. This algorithm was tested extensively using the broad cross-section of images and compared to the results of state-of-the-art 2D ADR techniques. These tests revealed three clear advantages of using 3D ADR. First, the 3D algorithm demonstrated improved detection of the material anomalies when compared to the 2D algorithm. In particular, several synthetic hard

alpha targets with low reflectivity that were not detected with the 2D ADR approach were detected using 3D ADR. Second, 3D ADR reduced FP inspection results due to titanium (Ti) microstructure. The FPs increased the cost of ultrasonic inspection by causing the unnecessary scrapping of good material. The third advantage of 3D ADR was that larger volumes of material could be inspected while maintaining the same sensitivity as 2D ADR, which could lead to improved productivity for the inspection of aerospace billet and forgings.

The prototype 3D ADR algorithm was ported to a C++ library suitable for industrial implementation. A test harness for the C++ library was written in Java using the open source ImageJ platform. Writing the industrial version of the software as a multitiered application enables it to be reused easily by ultrasonic equipment vendors. The industrial software had a 9-minute execution time for data files collected from a typical aerospace forging. This execution time can be reduced by porting the C++ library to a low-cost, high-speed computing platform using graphics processing units or a parallel processing, multithreaded architecture using multiple central processing unit cores. Implementation on a high-speed computing platform was beyond the scope of this program.

Finally, a demonstration of the 3D ADR technology was held in an environment representative of production ultrasonic inspection for aerospace forgings. An NAS 401 certified level II operator used a commercial off-the-shelf 3D ultrasonic data acquisition system from OKOS Systems to scan a small Ti forging with synthetic targets. Complete 3D ultrasonic data were collected at over 20″ per second surface speed. The performance of the mechanical system limited the speed to 20″ per second. Surprisingly, the ultrasonic data acquisition system did not limit the data acquisition speed and could support higher speeds than those demonstrated. The level II operator used the 3D ADR industrial software to analyze the data. The 3D algorithm demonstrated the improved results over the 2D algorithm in this production-representative environment.

1. INTRODUCTION

Studies have shown that ultrasonic testing (UT) results, like many nondestructive testing (NDT) methods, are dependent on operator interpretation of the inspection results. In an effort to minimize the variability introduced by operator interpretation, image-processing technology has been applied to NDT results. Inspections incorporating this technology are referred to as either automated defect recognition or assisted defect recognition (ADR), depending on the level to which the operators are involved in the process. The ADR algorithms applied to industrial UT inspection use only the data available in two-dimensional (2D) C-scans to detect indications. This approach has proven to have a high probability of detection (POD), but false positives (FPs) can result because acceptable but highly reflective grains in metallic microstructures cannot be correctly classified any differently from voids or inclusions based on 2D data alone. Because of limitations in computing power and data storage, commonly used industrial UT inspection systems have traditionally been limited to stop-on-defect or C-scan data acquisition. With the improvements in computational power and data storage within the computer industry, the next generation of UT inspection equipment should have the capability to analyze and archive three-dimensional (3D) A-scan data in production environments. This evolution from 2D to 3D ultrasonic data will provide more information for both improvements in detection and proper classification of material anomalies.

The focus of this program was to examine the feasibility of using 3D ultrasonic data by extending successful 2D ADR concepts to 3D ultrasonic data sets and demonstrating the potential benefits to the industry in terms of increased detection of melt-related defects and a reduction in FP indications from acceptable microstructures. This research is timely for the industry for several reasons. With the increase in fuel costs, new engine designs will need to provide improved fuel efficiency. Increasing the POD for melt-related defects will enable the engineering teams to consider more fuel-efficient designs. With the recent increases in raw material cost within the aviation industry, reducing the number of FP indications has the potential to significantly impact manufacturing costs. Also, a large portion of the current UT equipment in the industry is 10 to 15 years old and nearing the end of its usefulness. Providing the industry with demonstrations of improvements in both cost savings and inspection quality, 3D UT data analysis techniques have the potential to provide the industry with sufficient substantiation to justify planned reinvestments in new equipment that can take advantage of the increased data analysis methods that ADR provides.

This program was divided into three major tasks. The initial task centered on collecting the UT data necessary for the development of the 3D ADR software. The fabrication of specific test specimens for ADR was not within the scope of this program. Instead, the team used specimens identified in other Federal Aviation Administration (FAA) programs, such as the Contaminated Billet Study (CBS) [1] and the synthetic inclusion disk created and used under the Engine Titanium Consortium [2], or pre-existing specimens from General Electric (GE®) Aviation or other aviation power plant original equipment manufacturers (OEM). While the program's main focus on samples for 3D ADR was for titanium (Ti) alloys, specimens of nickel-based alloys were also examined. The team devised a set of ultrasonic data acquisition parameters based on common industry testing practices for aerospace alloys. Instead of stop-on-defect, or C-scan data acquisition, complete A-scan waveform data were collected with those parameters to allow

3D ADR algorithm development. The specimen data were collected at GE laboratory facilities at the GE Aviation Quality Technology Center (QTC), located in Cincinnati, Ohio, and the GE Global Research Center, located in Niskayuna, NY.

During the second task, prototype 3D ADR approaches were investigated and evaluated. To facilitate rapid prototyping, a commercially available fourth-generation language (4GL) was used for the software development during this task. The software used for the program was Interactive Data Language (IDL®), produced by Exelis Visual Information Solutions [3]. The software includes 3D image-reconstruction algorithms to create image data sets from the ultrasonic waveform data that are suitable for ADR and the ADR processing algorithms for the 3D image data. The ADR processing algorithms were evaluated on the data collected during the initial task for improved detection of material anomalies and discrimination of material anomalies from material noise.

The third task was to conduct a technology demonstration with the goal of demonstrating the successful implementation of the technology in a production-representative environment. The prototype software created and used internally by GE Aviation for the previous task to demonstrate technical feasibility was not designed for a technology demonstration in a production-representative environment. As a tradeoff for the ability to rapidly prototype algorithms, 4GL software packages do not provide the computational efficiency necessary for use in an environment representative of production ultrasonic inspection. As part of this task, the algorithm developed in the previous task was ported to a platform suitable for the demonstration. The user interface was implemented using the open source ImageJ software from the National Institutes of Health (NIH) [4]. The computational algorithm was migrated to C++ using Microsoft® Visual Studio®. Based on the results from the previous two tasks, the synthetic inclusion disk (SID) was selected as the test specimen for the demonstration. An ultrasonic scan plan using the 3D data collection was developed for this disk forging, using the OKOS NDT System [5] located at GE Aviation laboratory facilities in Cincinnati, Ohio. The technology demonstration was conducted on February 6, 2013. It was attended by aviation power plant OEMs, ultrasonic inspection suppliers, and ultrasonic equipment vendors.

The balance of this report will provide detailed descriptions of those three tasks and some supporting details regarding the technical working group (TWG), technology transfer, and software design.

2. THE TWG

GE Aviation and the FAA worked together to create a TWG for this program. The TWG was formed from a volunteer group of aviation industry NDT experts. The role of the TWG is to:

- Provide peer review of technology plans and progress.
- Offer suggested improvements based on diverse perspectives and experience.
- Identify requirements for widespread adoption of the technology.

With input from the FAA, GE invited industry members to participate in the TWG at the start of the program. The TWG invitations were extended to representatives of the government, engine

OEMs (GE, Rolls-Royce® plc, Honeywell® Aerospace, and Pratt & Whitney), suppliers of billets (TIMET, Allvac, etc.), suppliers of disk forgings (Wyman Gordon, ChenTech, etc.), independent inspection vendors (Hansen Aerospace, Acuren, etc.), and inspection system commercialization sources (GE Inspection Technologies, UTEX, etc.).

During the program, five TWG meetings were held: (1) a kickoff meeting to review program objectives and solicit participation; (2) a technical review of samples to be used for ultrasonic data collection; (3) a review at the end of the first year of the program to demonstrate feasibility; (4) a technical review of the plans for the technology demonstrations, and (5) the technology demonstration. The members of the TWG are listed in table 1.

Table 1. The TWG Members

Name	Company
Pat Howard	GE Aviation
Andy Ferro	GE Aviation
Rich Klaassen	GE Aviation
Al Klassen	GE Aviation
Cu Nguyen	FAA
Waled Hassan	Rolls-Royce plc
Jeff Umbach	Pratt & Whitney
Jon Bartos	Cincinnati Aerotech Consulting
William Wee	University of Cincinnati
Steve Pajka	Hansen Aerospace
Mark Turner	GTI
Bruce Boris	Timet
John Eads	Acuren
Bill Kanner	Acuren
Tom Sharp	Etegent Technologies
Sue Montagna	GE Inspection Technologies
Krishna Mohan Reddy	Lucid Technologies

3. PROGRAM METRICS

A method for measuring success is important for any technical program; this program is no exception, so the team established performance metrics for the ADR software early in the process. The metrics for tracking performance of the ADR algorithms for this program are centered on three measurements that will be discussed in detail: the difference between the estimated signal-to-noise ratio (SNR) and the ground truth SNR, the FP rate, and the true positive rate (TPR).

3.1 THE SNR

The program will use the definition of SNR that has been used previously in the FAA-sponsored Engine Titanium Consortium programs [2]. Equation 1 defines SNR as:

$$SNR = \frac{P_s - \mu_n}{P_n - \mu_n} \tag{1}$$

where P_s is the peak value of the signal, P_n is the peak value of the homogeneous noise surrounding the indication, and μ_n is the mean value of the same homogeneous noise region. Figure 1 contains a region of interest (ROI) from an ultrasonic image with an indication and an area of homogeneous noise surrounding the indication. The value of P_s would be the maximum value of the ROI surrounding the signal, and P_n and μ_n would be calculated from the remaining homogeneous noise with the signal ROI removed.

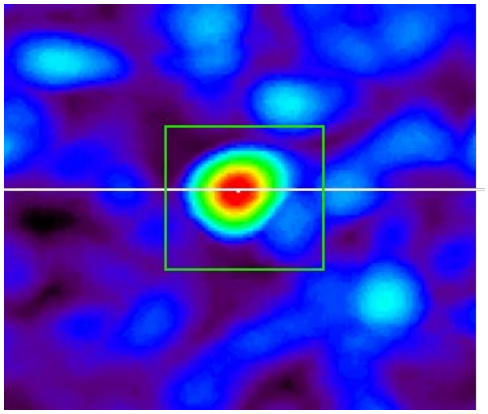

Figure 1. The ROI Containing Ultrasonic Indication in Homogeneous Noise

The primary metric around SNR is not the SNR itself, but the accuracy of the SNR calculated by the ADR software when compared with ground truth. The SNR error is defined as $|SNR_M - SNR_{GT}|$ where SNR_M is the measured SNR produced by the SNR algorithm and SNR_{GT} is the ground truth SNR for that indication.

The ground truth SNR is defined as the SNR calculated by the GE Aviation 2D ADR software. The SNR calculation in this software was validated on over 10,000 ultrasonic images and compared to the SNR values measured by certified level II ultrasonic operators using the following criteria:

- P_n within ±6dB of P_n in signal ROI
- μ_n within ±2dB of μ_n in signal ROI
- At least 5000 pixels in the homogeneous noise ROI
- Homogeneous noise ROI not to exceed 1200 pixels in the scan direction

Figure 2 shows an example of the ground truth criteria applied to an ultrasonic image.

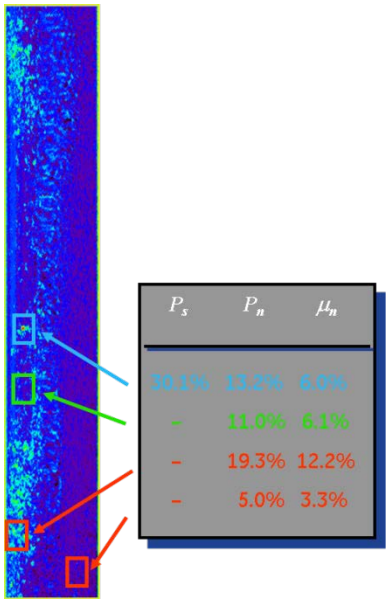

Figure 2. Example of Ground Truth SNR Criteria

The most effective method of comparing the 3D ADR software's SNR to the ground truth SNR is graphically, as shown in figure 3, where the 3D SNR is located on the vertical axis and the 2D ground truth SNR is located on the horizontal axis; the 45° line is the line of equivalence for the 2D and 3D SNR values. If a detection threshold in terms of SNR is overlaid on this plot, four quadrants are created. The most interesting quadrants are the upper-left and lower-right quadrants. If a data point falls in the upper-left quadrant, this indicates that it was detected using 3D ADR, but missed using 2D ADR. This is the quadrant of improved performance for 3D ADR. Conversely, if a data point falls in the lower-right quadrant, it was missed by 3D ADR and detected by 2D ADR. This is the quadrant of degraded performance for 3D ADR. Plots such as the one in figure 3 will be used extensively to evaluate the performance of the 3D ADR software.

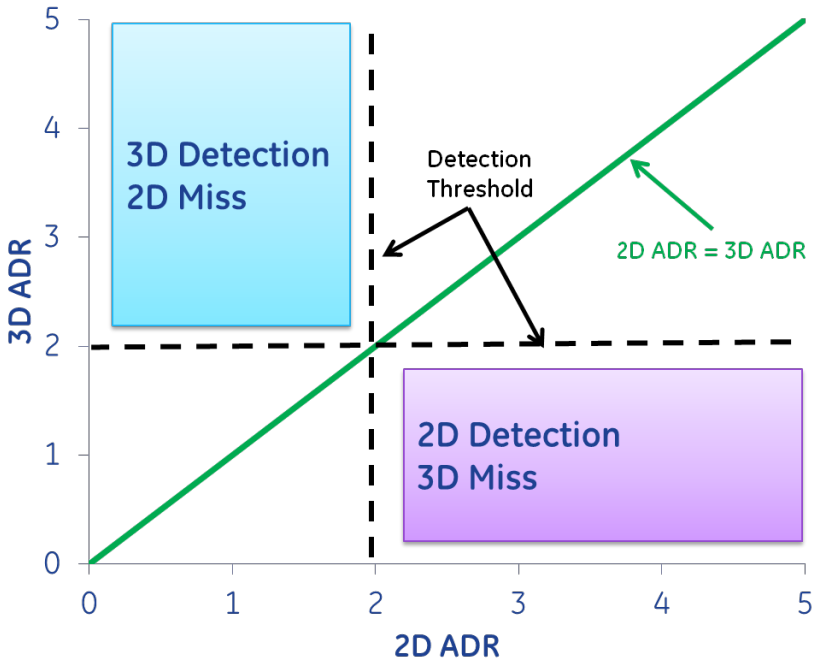

Figure 3. Example Plot of 3D SNR Compared to 2D SNR

3.2 RECEIVER OPERATING CHARACTERISTIC CURVES

The program will also track the FP and TPRs for the candidate 3D ADR algorithms. An FP occurs when the measured SNR, SNR_M, for an indication calculated by the ADR algorithm is greater than the SNR threshold, SNR_T and the indication does not correspond to one of the known targets in the test specimens. A true positive (TP) occurs when both SNR_M and SNR_{GT} are greater than SNR_T and the indication corresponds to a known target. Negative inspection results may be classified as a false negatives (FN) or true negatives (TN). An FN occurs when SNR_M is less than SNR_T and the indication originates from one of the known targets. A TN results when SNR_M is less than SNR_T and the indication does not correspond to a known target. These terms are summarized by the matrix shown in figure 4, which is often referred to as a truth table.

Truth \ ADR	Defective	Good
Defective	True Positive	False Negative
Good	False Positive	True Negative

Figure 4. Summary of Inspection Result Terminology

The TPR is the number of TP results divided by the total number of opportunities (where $SNR_{GT} > SNR_T$). Similarly, the false positive rate (FPR) is the number of FP results divided by the number of opportunities (where $SNR_{GT} \leq SNR_T$).

Using the receiver operating characteristic (ROC) curve is a graphical way to compare the performance of two systems in terms of TPR and FPR. The ROC curve is parametric; the FPR is plotted on the *x*-axis and TPR on the *y*-axis, and a parameter of interest, such as threshold, is varied to create the curve. Figure 5 shows an example of an ROC curve.

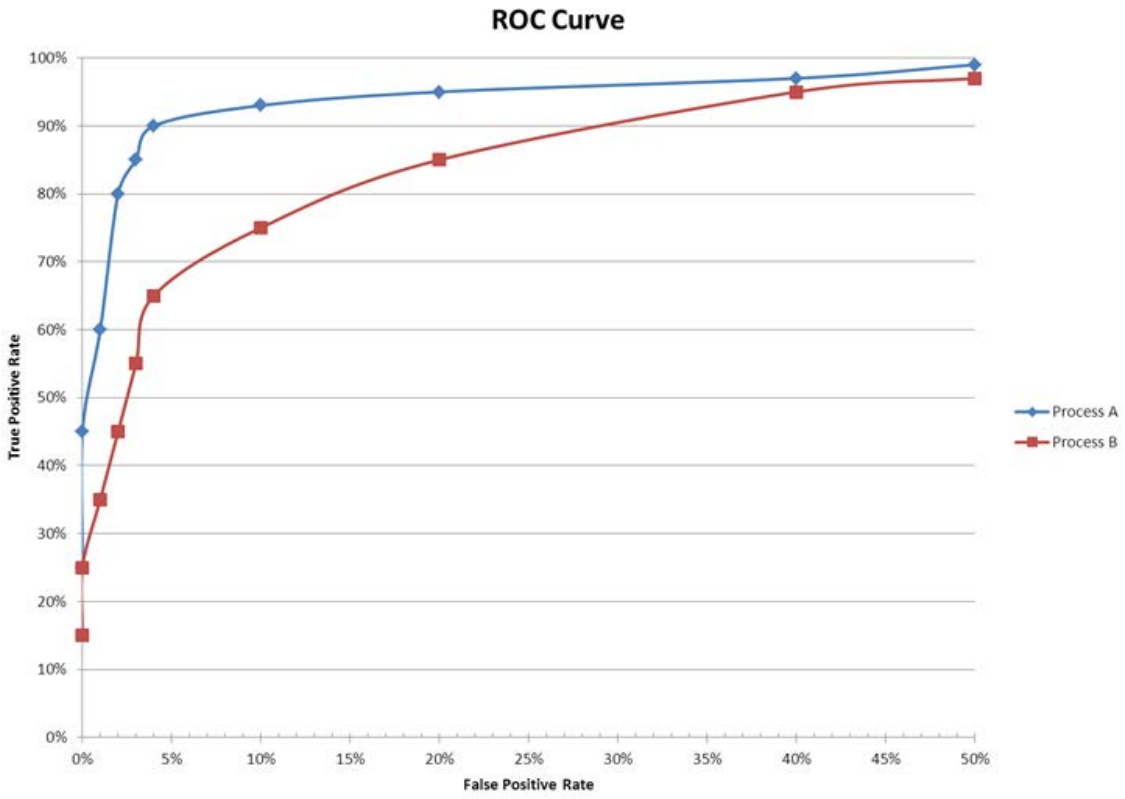

Figure 5. Example of ROC Curve

An ROC curve is not defined in terms of multiple positive test results for a single image. We anticipate test images in this program having multiple indications per image. A free-response ROC (FROC) curve is functionally similar to an ROC curve, but allows for the possibility of multiple TPs per image. This program will use FROC curves to communicate the performance of ADR algorithms.

4. ULTRASONIC DATA COLLECTION

Although ultrasonic data acquisition was not the primary focus of this program, it required the collection of ultrasonic data sets to support the development of the 3D ADR software. The test specimens identified for use in the program are described in section 4.1. The ultrasonic data acquisition parameters that were applied to the specimens are defined in section 4.2.

4.1 TEST SPECIMENS

There was no specific task in this program for the creation of test specimens specifically designed and manufactured for ADR software development. Instead, the test specimens used

were created from previous FAA-funded programs and naturally occurring indications made available by TWG members. The team identified the list of test specimens described in tables 2, 3, and 4. Table 2 contains manufactured test specimens. Tables 3 and 4 contain naturally occurring indications provided by GE or other TWG members.

The manufactured test specimens in table 2 were created during the FAA Engine Titanium Consortium program [2]. These specimens were manufactured from Ti alloys sectioned from rotating disk forgings. As a result, the blocks retain the flow lines from the forging process and the resulting variable grain noise patterns. The blocks with flat bottom hole (FBH) targets manufactured with holes located at 1″ and 2″ metal travel from the top surface of the specimen. Each specimen has eight repeats of four different target sizes for a total of 32 targets. The four sizes for the FBH targets were 4/64″ (#4), 3/64″ (#3), 2/64″ (#2) and 1/64″ (#1) in diameter. The targets were manufactured on a regular grid. Another set of specimens was manufactured with synthetic hard alpha (SHA) inclusions. These inclusions were inserted into the test specimen with 2″ metal travel from one surface and 1″ metal travel from the opposite surface so the test specimen can be inspected from both surfaces. The SHA specimens also have the 32 target pattern. The sizes of the targets were 5/64″ (#5), 4/64″ (#4), 3/64″ (#3), and 2/64″ (#2) in diameter. The targets were manufactured with different ultrasonic reflectivities by varying the percentage of nitrogen content in the inclusions. While these blocks were used for this program to control costs, they are not ideal for ADR algorithm development. The large quantity of targets in a small area is not representative of how indications occur in production aerospace components.

Table 2. List of Test Specimens With Artificial Targets

Serial Number	Target Type	Composition	Orientation	Alloy	Owner
SA940512-2.8N	SHA	2.8%N	45°	Ti6-4	FAA
SA941201-2.8N	SHA	2.8%N	45°	Ti-17	FAA
SA950320-5.2N	SHA	5.2%N	90°	Ti-17	FAA
SA950317-5.2N	SHA	5.2%N	45°	Ti-17	FAA
D950209-5.9N	SHA/WC	5.9%N	90°	Ti6-4	GE Internal
F931213-2.5L	FBH	-	90°	Ti6-4	GE Internal
F931213-1.5L	FBH	-	90°	Ti6-4	GE Internal
F931213-1.5S	FBH	-	45°	Ti6-4	GE Internal
F950508-1.5S	FBH	-	45°	Ti-17	FAA
F950508-2.5S	FBH	-	45°	Ti-17	FAA
F950508-2.5L	FBH	-	90°	Ti-17	FAA
F950508-1.5L	FBH	-	90°	Ti-17	FAA
S940119-1.6N	SHA	1.6%N	90°	Ti6-4	FAA
S940128-2.6N	SHA	2.6%N	90°	Ti6-4	FAA
S940217-5.9N	SHA	5.9%N	90°	Ti6-4	FAA
SA940314-5.2N	SHA	5.2%N	45°	Ti6-4	FAA
SA940513-1.5N	SHA	1.5%N	45°	Ti6-4	FAA
S941202-2.8N	SHA	2.8%N	90°	Ti-17	FAA
901004-1L	FBH	-	90°	Ti6-4	GE Internal
901004-2L	FBH	-	90°	Ti6-4	GE Internal
S950316-1.5N	SHA	1.5%N	90°	Ti-17	FAA
SA950321-1.5N	SHA	1.5%N	45°	Ti-17	FAA
SID	SHA	Various	Various	Ti6-4	FAA

Table 3. List of Non-Billet Test Specimens With Naturally Occurring Targets

Current Geometry	Material	Type
Disk	Ti-17	Void
Shaft	Inco718	Void
Disk	Inco718	Void
Ring	Ti	Grain
Ring	Ti	Grain
Disk	Ti-6242	Grain
Cutout	Ni	Void
Cutout	Ti	Real
Cutout	Ni	Void
Cutout	Ni	Real
Cutout	Ni	Surface Finish
Cutout	Ni	Real
Cutout	Ni	Real
Cutout	Ti	FBH

Table 4. Detailed Description of Naturally Occurring Billet Test Specimens

Diameter	Material	Length	Indication	Amplitude	SNR	Zone	Axial Location	Comment
6″	Ti-17	36″	1	98%	6.7	3, 4	2.25″	
			2	74%	11.0	2, 3	10″	
			3	96%	10.5	2, 3, 4	18.5″	
			4	100%	6.6	2, 3	27.5″	
6″	Ti-17	36″	1	+5.5dB	11.5	2, 3	6.5″	
			2	60%	6.1	2, 3, 4	10.3″	
			3	45%	6.5	2, 3	29.9″	
8″	Ti-6242	10″	1	39%	3.4	1	5″	
6″	Ti6-4	74″	1	63%	3.0	4		CBS Billet – B1BW1A
			2	113%	5.7	3		
			3	142%	8.1	1		
			4	56%	2.8	2		
			5	69%	3.1	2		
			6	450%	26.6	2		
6″	Ti6-4	34″	1	73%	2.45	4		CBS Billet – B3W1BB
			2	99%	3.5	4		
			3	134%	9.5	3		

4.2 DATA ACQUISITION

The team chose to break the data acquisition problem down into two different components: target SNR and the qualitative spatial pattern of the noise. The team identified three different ranges of SNR to acquire: low (less than 2.5), medium (between 2.5 and 3.5), and high (greater than 3.5). Likewise, three types of noise patterns were identified: uniform (low), variable (high), and banded, producing the opportunity for target signals on the edge of the noise bands. The intersection of these classes produces the opportunity to produce nine different types of images, as shown below in table 5. The team established a goal of collecting 10 to 12 images of each of the nine types shown in the table.

Table 5. Matrix of Nine Image Types for Data Acquisition

		Noise Pattern		
		Uniform	Variable	Edge Target
SNR	SNR < 2.5			
	2.5 < SNR < 3.5			
	SNR > 3.5			

The challenge for the team was finding a way to collect the required file types and quantities, given the limited number of test specimens available to the program and the inability to create new specific test specimens. The team took the approach of varying the ultrasonic data acquisition parameters, such as frequency, focal length, waterpath, and time-corrected gain settings, to create multiple images that meet the criteria described above from a single test specimen. This approach is illustrated in figure 6.

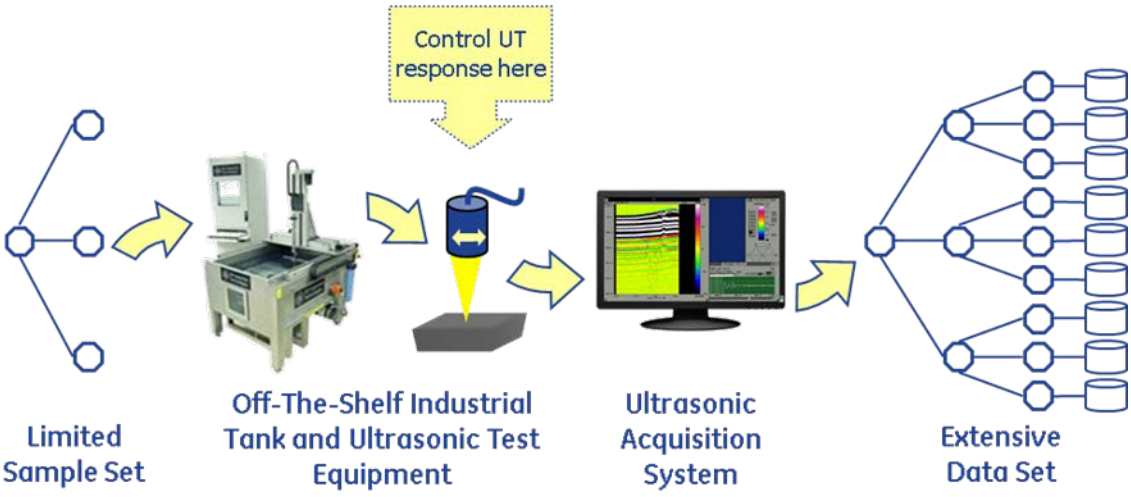

Figure 6. Approach for Producing an Extensive Data Set From a Limited Set of Test Specimens

For example, in a uniform noise specimen, the SNR of the target can be varied by changing the frequency of the transducer in the range between 2 MHz and 10 MHz. In a variable noise

specimen, refracted longitudinal waves can be used instead of longitudinal waves to create a banded noise pattern.

In total, 195 data files were compiled on the collection of test specimens. The complete list of data files and the associated parameters can be found in appendix A. Each of the data files was classified using the scorecard from table 5. The results of the scoring are found in table 6. A significant number of files were generated for six of the nine categories. Additional files in the edge target category were desired, but those types of targets do not occur often.

Table 6. Number of Ultrasonic Images Collected by Type

		Noise Pattern		
		Uniform	Variable	Edge Target
SNR	SNR < 2.5	24	12	1
	2.5 < SNR < 3.5	18	12	1
	SNR > 3.5	25	5	3

5. SOFTWARE DEVELOPMENT

The major output of this program was the software to implement the ADR algorithm. There were two phases to the software development: rapid prototyping and production demonstration. These two phases are described in detail in the following sections.

5.1 RAPID PROTOTYPING SOFTWARE

The IDL software package was selected for the development of the prototype ADR software. IDL is a 4GL programming language for creating data analysis software. It is available for purchase from Exelis Visual Information Solutions [3]. A prototype software package was developed for the purpose of loading, analyzing, and performing calculations on 3D ultrasonic data acquired from samples of nickel and Ti alloys. The software, the function of which was to be a test harness for the development of the 3D ADR investigation, was designed for generality with respect to ultrasonic signals and the application of ADR. As such, the software contains as many software inputs (or hooks) as possible for the signal processing engineer to adjust, resulting in a highly customizable development platform for testing the performance of 3D ADR. Figure 7 shows a screen shot of the test harness.

5.1.1 Input Data

The software takes 3D radio frequency (RF) waveform data as input from off-the-shelf ultrasonic data acquisition systems, set up in pulse-echo mode. Figure 7(a) shows the data input interface. The input data need to be organized as a 2D array of A-scan waveforms. Each waveform contains the received amplitude of the sound wave as it travels into the test component, at every (x, y) position of the scan. The raw data are assumed to be unrectified, representing the material structure of the part, convolved with the impulse response of the ultrasonic transducer. The input data are assumed to be digitized on an 8-bit scale and the digital spatial resolution of the

data is allowed to vary based on the scan and index sample sizes at the time of acquisition. The software assumes that the digital resolution of the input data is appropriate for the transducer properties, material properties, and desired signals to obtain.

5.1.2 Rectification

The test harness contains a data rectification algorithm as an optional preprocessing step for analysis. Figure 7(b) shows the rectification control. The rectifier's function is to eliminate the responses from the specific transducer that acquired the data, leaving only the data that represent material response. It works by mixing the raw quadrature and in-phase waveforms to baseband, using the transducer transmission frequency as input. A standard low-pass filter eliminates the resulting harmonics and the waveforms are recombined to form the rectified signal. This process repeats for all of the A-scans.

5.1.3 Gating

The test harness contains hooks for digitally segmenting the RF data into multiple C-scan images that can be used to create a volumetric image, as shown in figure 7(d). The data can be partitioned into gates by selecting the number of RF samples desired in each gate. Gate 0 can be defined to start at any sample number, removing any undesired data at the beginning of the waveforms (for instance, to eliminate a front wall signal that should not be analyzed). Similarly, gate N can be defined to end at any sample number, removing data at the end of the waveforms.

5.1.4 Display

The data are displayed in the prototype as slices within the 3D volume. As stated above, the 3D volume is acquired as a 2D array of A-scans. The acquisition system acquires a single line of A-scans in a single scan, then indexes to the next line to acquire the next scan. Each line of A-scans is viewed as an image slice, a B-scan, as if the part were cut vertically and the underlying slice of material were seen. The stack of B-scans is shown in the viewer, as seen in figure 7(e). The vertical profile or column of data on a B-scan slice can be plotted as an A-scan, as shown in figure 7(g).

Likewise, the data are sliced in the horizontal direction and viewed as C-scans, as shown in figure 7(f), representing the data within each gate. Each point in the C-scan is defined as the maximum amplitude of the (x, y) A-scan within its respective gate. The number of gates determines the number of C-scans. The A-scan represented by a single pixel in the C-scan can be plotted as an A-scan in the viewer, as well as the B-scan corresponding to a single row in the C-scan.

The B-scan and C-scan displays in the view have control to set the color palette and adjust the contrast, as shown in figure 7(h).

5.1.5 The ADR Algorithm

A 3D ADR algorithm, which degenerates to the 2D algorithm when the entire volume has been gated, has been integrated into the test harness through the control shown in figure 7(c). Every parameter that defines the algorithm's behavior has been exposed in the software for customization in figure 7(d). The ADR's function is to determine the signals within each C-scan that exceed predefined SNR criteria, based on the local neighborhood of data surrounding each signal in two dimensions. The parameters that control the detection of the signals and the parameters that control the SNR classification of the signals are tunable. When the algorithm is executed, the set of 2D images is searched for such signals that exceed the SNR criteria and the results are displayed. Additionally, annotations can be overlaid on the C-scan images, describing the signals determined and their respective noise regions used in the calculation of the SNR.

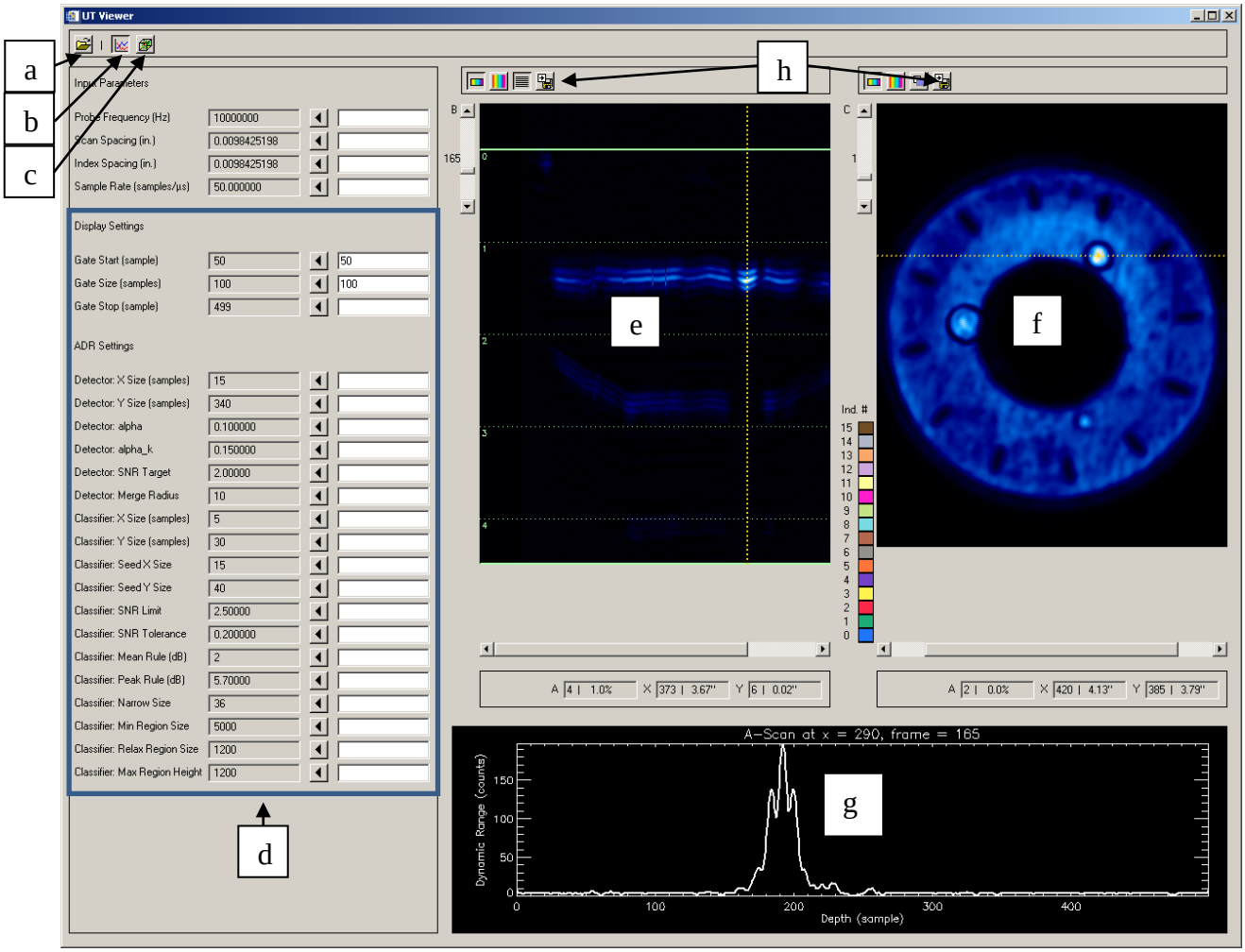

Figure 7. Screenshot of the 3D UT ADR Test Harness: (a) File Importer, (b) A-Scan Rectification Function, (c) ADR, (d) Tunable Parameters for C-Scan Generation and ADR Settings, (e) B-Scan Viewer, (f) C-Scan Viewer, (g) A-Scan Viewer, and (h) Image Color Palette

5.2 PRODUCTION DEMONSTRATION

The management of the software portion of the 3D ADR program used, in general, the waterfall approach to a software development life cycle. The steps involved included the requirements, analysis, design, implementation, and testing phases. During the requirements phase, a design of experiments (DOE) was performed to determine the critical factors associated with the ADR algorithm with respect to the types of data expected. The factors included gate size and sub-image sizes for the detector; and sub-image sizes, gating criteria, and region-growing parameters for the classifier. The final list of parameters was determined to have a large effect on the calculated SNR. During the analysis and design phases, a prototype was developed, as described above. The prototype was developed with the advantage of requiring little programming time to integrate the needed components for testing ADR algorithms. This test harness allowed for the quick analysis of the data that was being generated and changes to the algorithms to be made quickly. What resulted from this process was a design that could be implemented in software architecture more readily adapted for use in the industry. During the implementation and testing phases, the software architecture was designed, requiring the optimal configuration for 3D ADR to be implemented in the field. The software architecture determined was a 3-tier approach, which separated the GUI, algorithms, and data access. Reusable software was also required, so many industry users could easily use it in their own packages.

5.2.1 Multitier Software Architecture

Multitiered software is a software design pattern that uses data abstraction concepts to logically separate the key sections of the software. For example, in three-tiered architectures, there is a presentation tier, a business logic tier, and a data tier. These tiers, also sometimes called layers, serve as separate modules that can be interchanged without affecting any of the other tiers. To do this, multitiered architecture designs set up agreed-upon client/server protocols to communicate information to the adjacent tier. As long as those communication protocols are adhered to, interchangeability is maintained without the need for any other tiers for one to know the other's implementation details.

Advantages of the multitiered architecture include maintainability, scalability, and security. Each tier can be modified without changing the others, increasing the maintainability of small sections of software. Each tier is independent of the others, meaning that any of the tiers can be scaled to meet the requirements of the application without affecting the rest of the software. Each tier is in control of the tier below and above and has no access to the others. This concept increases security.

5.2.2 Reusable Software Model

The reusable software model is also a design pattern, which eliminates the need for reinvention and rediscovery. Fitting with a multitiered approach, the cornerstone of reusable software is a modular paradigm. The software must have decoupled components, meaning that interconnections between components are minimized. Likewise, components must be highly cohesive, meaning that a module performs only one task. Finally, data abstraction completes a

modular design by hiding error-prone operations from other modules and exposing only the communication protocols to calling methods.

Advantages of code reuse include reliability, extensibility, accessibility, efficiency, and portability. Each component is fully tested to make it reliable, robust, and available. Reusable code is extensible because quick updates to changing requirements can be made without affecting the entire application. This optimizes efficiency, decreases development time, and increases system performance. Also, reusable code is portable to support many applications.

5.2.3 Reference Implementation

The result of the software architecture described makes it possible to deliver a reference implementation to the industry, which provides a presentation tier, a business logic tier, and a data tier. The presentation tier consists of the reference implementation, which can be thought of as an example to the industry for how to integrate 3D ADR into an ultrasonic acquisition application. The reference implementation is a bare bones program, which provides only the functionality needed to call the 3D ADR algorithm and nothing more. It is not intended to be a full-featured user interface.

The reference implementation was carried out in an open source code platform for optimal portability. The open source project called ImageJ is a standard in the image processing community. Because ImageJ is implemented in the Java programming language, and 3D ADR was implemented in C++ for computational reasons, this implementation also demonstrates the multilanguage capability of calling the C++ algorithms from Java. Figure 8 shows the interface to the reference implementation.

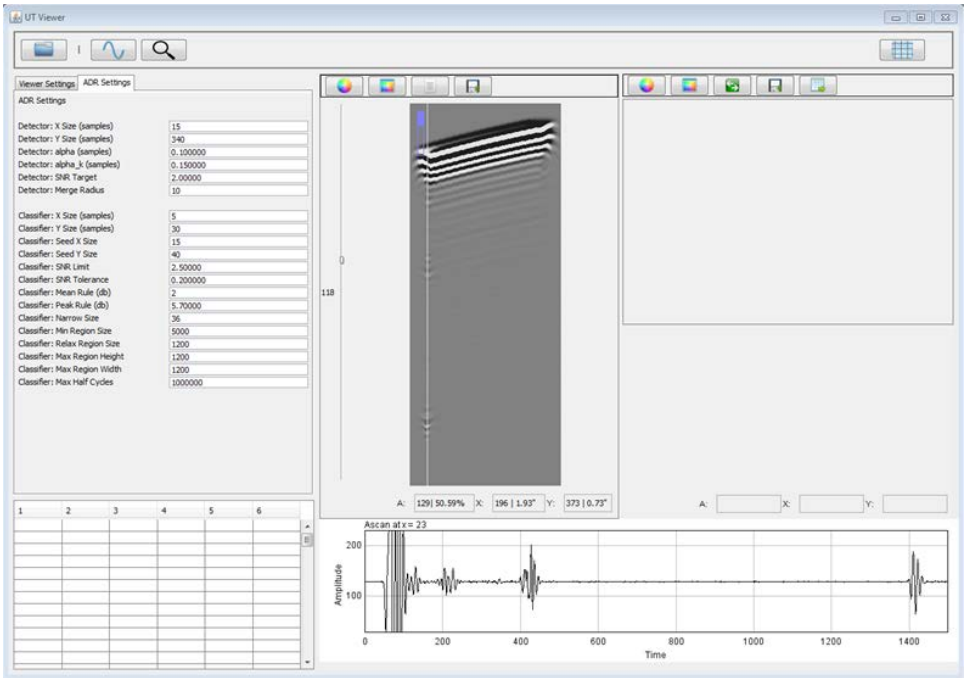

Figure 8. Graphical User Interface for the Reference Implementation Written With ImageJ

The presentation tier reference implementation is connected to the business logic tier which, in this case, is the algorithm library containing 3D ADR. As stated above, this tier is written in C++ and compiled into a Direct Link Library (DLL) for code reuse. The design allows for the ImageJ presentation tier to be replaced by an industry-specific presentation tier. The only requirement is that the communication protocols to the business logic tier must be adhered to. These protocols are defined in the DLL headers.

The business logic tier makes extensive use of the data tier—in this case, a third-party, open-source library of mathematical and image processing functions called VxL. Analogous to the other tiers of the architecture, the algorithm library adheres to the communication protocols defined by VxL. VxL can be accessed as an open source package at http://vxl.sourceforge.net/.

The chosen architecture, including a multitier approach and a reusable model (as shown in figure 9), includes many benefits. The decoupled ADR algorithm makes it simple for ultrasound acquisition vendors to integrate into their analysis packages. The reference implementation serves as an example of how to call the ADR algorithm. It can also be used as a starting point for new analysis packages. The third-party, open-source imaging library is maintained by the imaging community, making it unnecessary for the application vendors to maintain the low-level functions that ADR relies on.

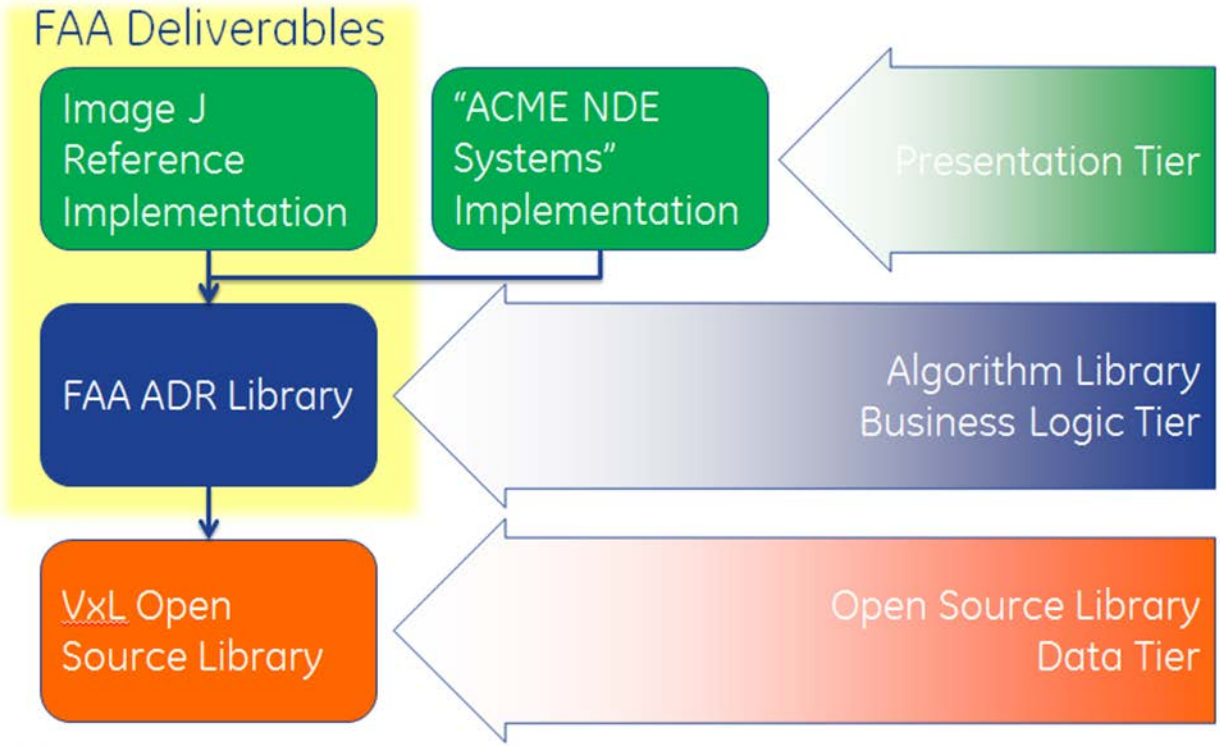

Figure 9. Multitier Architecture for Reference Implementation

5.2.4 Description of Deliverable Disk

The technical details of the project are available on the CD-ROM disk delivered as a result of the research in this report. The disk is divided into four sections:

1. The 3DUTADR—The business logic tier containing the ADR algorithm library, also referred to in the documentation as OpenNDE Lite. The directories in this section correspond to the C++ projects associated with the OpenNDE Lite algorithm library.

2. Documentation—Notes to a developer wishing to use the reference implementation or learn how to integrate ADR into his own software architecture.

3. The UT Viewer IDL—The prototype 3D ADR application written in IDL.

4. The UT Viewer Java—The reference implementation written in Java.

6. THE ADR ALGORITHM

Some high-level assumptions were made about the ultrasonic targets to be inspected using 3D ADR. These assumptions were used during the design and testing of the algorithm. The ROC analysis in this report assumes they hold. The ADR algorithm was designed to optimally find small indications, on the order of <0.125″ in diameter. It is assumed that large indications or strong reflectors are easily detected with a global threshold on the image in conjunction with operator review. Therefore, large areas of higher ultrasonic response will be considered background and not an indication area. Furthermore, in the presence of stringers, it is acceptable for ADR to detect a part of the indication and not the indication in its entirety. A stringer is defined as a dense grouping of indications that are, for example, organized in a line. It is assumed that the part must fail on the basis of partial conformance and must pass only on the basis of total conformance. Therefore, large areas of background surrounding the indication will be used for the SNR calculation.

6.1 DESCRIPTION

The objective of ADR is twofold: (1) to automatically detect defect indications hidden within the UT C-scan images, and (2) to classify these indications by their SNR levels, based heavily on the 2D ADR algorithm by Ferro and Howard [6]. Since the classification algorithm is designed to filter out potential indications that have been detected, the detection algorithm is tuned for a high overcall rate. Based heavily on the dynamic threshold algorithm [7], it works by generating a model of the C-scan background and comparing it to the actual signal frame. Because of the homogeneity challenges of forged Ti, the algorithm can be tuned for very high POD, but is limited to a relatively high FPR as well. Therefore, the detection results of the dynamic threshold are fed into an SNR classifier called Auto-SNR, which carefully determines a noise region to isolate only the indications that violate the SNR threshold by specification. This process of Auto-SNR is then extended above the indication in the gate dimension, and below, to calculate a 3D noise region for final SNR acceptance.

6.1.1 Detector, Dynamic Threshold

The dynamic threshold algorithm's goal is to produce a model of a given C-scan's background. More precisely, it provides a pixel-by-pixel threshold value, based on SNR, to detect outlying pixels, which will be called out as potential indications. Each pixel in the model, therefore, represents the highest amplitude its respective pixel in the C-scan can be without being part of a potential indication.

The algorithm, as described by Howard et al. [7], builds an array of Z-statistics from sub-image regions where sizes are a key design parameter. For high POD and high FPR on forging images, the optimal size was determined to be 15 x 340 pixels, based on results from a factorial DOE and the circumferential orientation of the typical background structure. All notable parameters in the algorithm have been exposed, however, for application-specific settings. Note that an improvement has been made to limit very small sub-images on the image edge, accounting for the image-dimension modulus in the horizontal direction: The horizontal size of the sub-image can therefore vary from image to image, shrinking if there are too few sub-images to create a background model. There must be at least three sub-images in either direction to create a model with at least one inflection point if one exists. The Z-statistics for each sub-image are defined by:

$$k_{i,j} = \frac{\max\left(X_{i,j}\right) - \mu_{i,j}}{\sigma_{i,j}} \tag{2}$$

where $X_{i,j}$ is the set of pixels in the (i,j)th sub-image. The array is then unwrapped and processed with a host of Infinite Impulse Response (IIR) and auto-regressive Finite Impulse Response (FIR) filters to back-calculate an expected peak signal using a rearranged version of equation 1. Pixel-by-pixel thresholds are obtained from a bilinear interpolation of the sub-image estimates. It is worth noting at this point that the smoothing steps, both of which, in conjunction, have the effect of spatially filtering the background model in sub-image space, are computationally far less expensive than the possibly more eloquent method of combining the filters and interpolation into a single 2D IIR filter. This would require an image-size multiplication of FFTs, as opposed to just a few operations in sub-image space. The dynamic threshold process is then repeated for all gates in the volume.

6.1.2 Auto-SNR

The indication mask from dynamic threshold is the key input to the Auto-SNR classifier, as described in Ferro and Howard [6]. The output is either equal to or a subset of the indications from this mask. To determine a reliable SNR for these indications, carefully devised rules generated by certified inspection experts must be employed on a spatially contiguous basis. The noise region, which is not limited to a rectangular box as in the manual process, must contain all homogenous and contiguous background, as defined by the noise levels in the proximity of the indication in question. The entire algorithm is repeated for each of the indications found in dynamic threshold, first on a 2D basis.

Because the noise region is a function of grouped statistics, namely mean, the image is divided into sub-images. As opposed to dynamic threshold, for this algorithm, it is important that the noise box strictly follow homogenous noise, which spatially varies suddenly in forged Ti. Therefore, the sub-image size is restricted to being as small as possible, especially in the horizontal direction or the direction orthogonal to the noise striations. The optimal setting, confirmed via DOE, is 5 x 30 pixels and tunable, where a mean with 150 data points is verifiably significant. Because the location of the indication is known, the grid is centered on the middle of the indication. This results in an optimal number of full sub-images closest to the indication, but implies that all four edges of the image can contain partial sub-images. Centering the grid on the indication also has the effect of providing more consequence to the indication's location relative to the surrounding background, as opposed to its location relative to the edge of the image. The result is an improved repeatability with respect to how the image has been acquired, where it was cropped, transducer position, etc. To increase the spatial significance of the sub-images for the purpose of tightly following the background structure, the sub-images are formed with 50% overlap in both directions. The sub-image regions are used to calculate a mean array and peak array in sub-image space, similar to the Z-statistic array in dynamic threshold. Some sub-images inevitably overlap with the indication in question. Overlapping and small edge cells are corrected a posteriori with a simple 8-nearest neighbor replacement algorithm. This replacement represents an estimate of what the background statistics would have been had they not been covered by the indication.

Now that the global statistics of the C-Scan are known, the noise region must be seeded so that the levels of the background to include in the noise region are known. The seed area is a tunable 15 x 40 pixel block centered on the highest amplitude pixel within the indication area. The area is used to determine the baseline mean and peak of the noise region at the indication location.

The initial noise region to be grown is based on the seed statistics. The noise box restriction rules, determined by experienced certified experts, are applied to both the mean sub-image array and peak sub-image array. Specifically, that is, any contiguous sub-image to the indication with a mean level within the range δ_μ of the seed mean level is used—and any contiguous sub-image to the indication with a peak level within the range δ_p of the seed peak level is used. Once the two arrays have been grown in this manner using connected components analysis, they are combined using a logical intersection,

$$R = \bigcup_{i\in\mu} M(i) \bigcap \bigcup_{i\in p} P(i), \mu = \left\{ x \middle| x = \mu_0 \pm \delta_\mu \right\} \text{ and } \mathrm{p} = \left\{ x \middle| x = p_0 \pm \delta_p \right\} \quad (3)$$

where M and P are the mean and peak sub-image arrays respectively, and are connected, and μ_0 and p_0 are the mean and peak values from the seeded region.

Noise regions are very sensitive to local maximums within the image and, as equation 1 implies, this makes forged Ti a difficult application to this model. Since the noise region has been grown in terms of sub-images, albeit small sub-images, it is possible that bits of bordering noise regions have been included in the one already computed. To limit this effect, the noise region is dynamically and morphologically eroded in sub-image space. Considering the fact that border pixels are not required for a conservative inspection as long as enough data points are included

for a reliable SNR calculation, this operation effectively shrinks the noise region to guarantee that it contains only intended pixels.

The result of this process is a stack of images corresponding to the noise regions for each indication at each gate. However, the noise regions are determined only in 2D. The next step is to grow these noise regions in 3D, starting from the indication location and working above and below the indication in a similar fashion to that described above. For a single indication, the seed peak and mean statistics surrounding the indication are first determined. Then, working contiguous to the indication gate, the 2D algorithm moves upward a gate and repeats the process for calculating a 2D noise region using the seed statistics and location as a starting point. Also working downward in gates, a 3D noise region is generated. The process of moving upward and downward stops when enough voxels have been included in the noise region or the growing stops as a result of the statistics themselves. The half cycles per gate are used as a measure of voxel limit, as this quantity is dependent on the transducer center frequency, f_c, used and its sample rate, f_s,

$$H = \frac{g + 2g_0}{f_s} \cdot 2 f_c, g_0 = 2\frac{f_s}{f_c} \tag{4}$$

where g_0 is the number of samples in the overlap region for gate calculation, or two cycles, and g is the number of samples per gate. In this experimentation, the total number of half cycles used was 1,000,000.

6.1.3 Algorithm Summary

Finally, given the output of dynamic threshold and Auto-SNR, whose sample results are shown in figure 10(b through d), ADR can calculate a final count of indications and their relevant statistics, such as SNR and peak amplitude. The SNR for each indication is, thus, calculated using equation 1. By discarding the potential indications with an acceptable SNR, Auto-SNR acts as a filter for dynamic threshold. In this way, a tolerance can also be built into the algorithm, simply by discarding indications that are below the specification SNR, less a tolerance. Also note that all relevant information regarding ADR output is contained in the indication and background masks, so in practice these should be saved for records retention and future calculations requiring SNR.

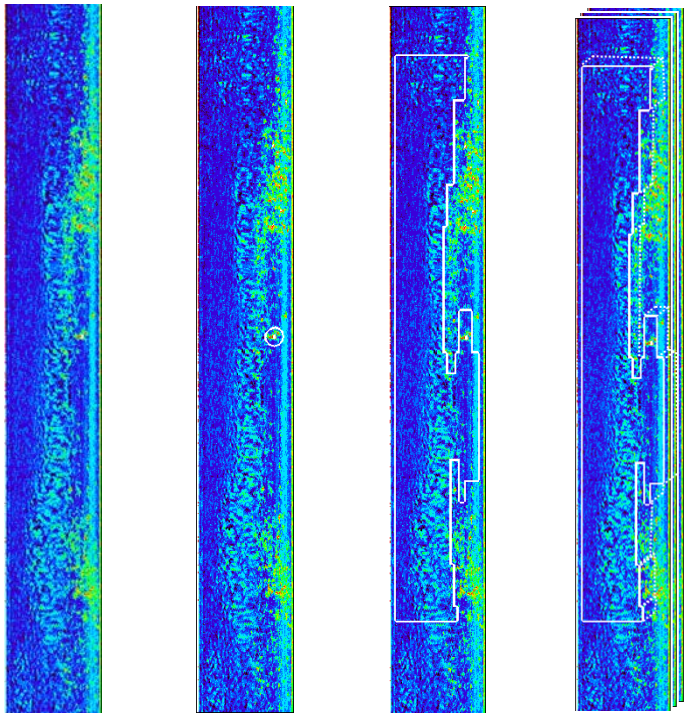

Figure 10. Example of C-Scan Images: (a) C-Scan Image With Two Possible Manually Drawn Noise Boxes Shown, (b) Output of Dynamic Threshold With the Indication Marked With a Circle, (c) Output of Auto-SNR With the Homogenous SNR Marked With an Outline, and (d) Output of Auto-SNR With Noise Region Expanded to All Gates

6.2 ALGORITHM TUNING

For the data examined in this study, typical values for parameters were discussed in the algorithm description. However, these values are not necessarily the best values for all types of data where ADR is required. For that purpose, all algorithm parameters were exposed for engineering design. These parameters are broken into two categories: detector parameters and classifier parameters (see tables 7 and 8). Factors to consider when adjusting these parameters include material microstructure, ultrasonic acquisition setup, part geometry, and image dimensions.

Table 7. Detector Parameters

Parameter	Description
X/*Y* size	Box size for subdividing image. Boxes are formed with 50% overlap.
Alpha	Defines the coefficients for the 2D FIR smoothing filter.
Alpha_k	Forgetting factor for the 1D IIR auto-regressive filter, traversing in an “s” pattern.
SNR target	The per-pixel SNR threshold for segmenting the indications into masks.
Merge radius	The radius in pixels of a disk surrounding the indication for merging nearby indications. Indications are merged when they are separated by a distance of 2 radii.
Transpose	Boolean for whether to transpose the C-scans before entry into ADR algorithm.

Table 8. Classifier Parameters

Parameter	Description
X/*Y* size	Box size for subdividing image. Boxes are formed with 50% overlap.
Aspect ratio optimization	Boolean for whether to recalculate *X*/*Y* size based on actual image dimensions to abate small subdivisions on edge.
Seed *X*/*Y* size	Box size for seeding the indication peak and mean statistics. Box is centered on the indication.
SNR limit/tolerance	The calculated actual SNR threshold for keeping indications in the report is limit minus tolerance.
Mean/peak rule	The value in dB for growing the noise region, using the seed statistics as a reference.
Narrow size	The minimum width of an image before special “narrow noise box growing” rules are applied.
Minimum region size	The minimum size for a noise region slice. If the region is too small, it is dilated independently of neighboring noise regions.
Max region height/width	The dimensions of the viewable area. The area limits the noise region from growing too far in either direction.
Max half cycles	The maximum number of transducer half cycles to include in the noise region before region growing is turned off. This effectively limits the noise region from growing in the depth direction.

6.2.1 Recommended Values

Given the data in this study, the following recommendations (tables 9 and 10) can be made as a starting point for engineering design of the algorithm for a specific application. Also provided is the motivation for setting the parameters.

Table 9. Recommended Detector Parameters

Parameter	Value	Comment
X/*Y* size	15, 340	Orient box in direction of background to model.
Alpha	0.1	Close to 0 → more aggressive filter; Close to 1 → less filtering.
Alpha_k	0.15	Close to 0 → more aggressive filter; Close to 1 → less filtering.
SNR target	2.0	Backed off from final SNR to find more potential indications.
Merge Radius	10	Set to be ~1/4″
Transpose	1	Circumferential direction should be *y*-direction, so transpose.

Table 10. Recommended Classifier Parameters

Parameter	Value	Comment
X/*Y* size	5, 30	Orient box in direction of noise box
Aspect ratio optimization	0	Needed only for very high aspect ratios (narrow images).
Seed *X*/*Y* size	15, 40	Orient box in direction of noise box; larger than *X*/*Y* size.
SNR limit/tolerance	2.5, 0.2	Final SNR to call out minus the tolerance.
Mean/peak rule:	2.0, 5.7	
Narrow size	36	Narrow image size in non-circumferential direction.
Minimum region size	5000	Number of pixels per gate to guarantee a significant SNR calculation.
Max region height/width	1200, 1200	Do not allow the size of the noise area to extend this far from the indication.
Max half cycles	10^6	Number of half cycles (RF A-scan) in 3D to guarantee a significant SNR calculation.

6.3 ALGORITHM PERFORMANCE

The algorithm performance, given four of the benchmark Ti FAA blocks, is described (S940128-2.6N, F9312113-2.5L, S950320-5.2N, and D950209-5.2N) and the SID, already presented in section 4.1. These specimens were scanned with optimal UT scan parameters and varying zone positions and depths. The scans were then analyzed with optimal settings for 3D ADR and optimal settings for 2D ADR for comparison. The specimens, as indicated, were scanned four times at different zone settings to test the algorithm, given various data sets. The gate type labeled conventional is the standard 1.5″ depth that is typical for conventional UT scans. An acquisition improvement is to reduce this zone size to 0.5″, as in the gate types labeled forging multizone (FMZ) centered and FMZ bottom, or FMZ scans centered on the indication and scans where the indication is located at the bottom of the zone. The FMZ centered zone is expected to show entitlement for the acquisition. Finally, the gate type labeled extended is the FMZ zone extended from 0.5″ to 1.0″.

6.3.1 Synthetic Inclusion Blocks

Figure 11 shows the results for the four gate types for the 2.6%N inclusion Ti block. It can be observed that many of the indications straddle the chosen 2D SNR operating point of 2.5, meaning that indications to the left of the line were detected by 2D ADR and indications to the right were not detected. The distribution of indications that straddle the 3D SNR operating point of 2.5 is less uniform. There are more indications above the line than below, meaning more were detected than not. Hence, the detection was better for the 3D algorithm. Indications on the SNR = 1 axes show that the indications were not detected at all and, therefore, were not measured. Note that there were three FP indications that the 2D ADR detected, but these same FPs were not detected by 3D ADR. This shows that, despite detection being better, the 3D algorithm also improved on the FPR.

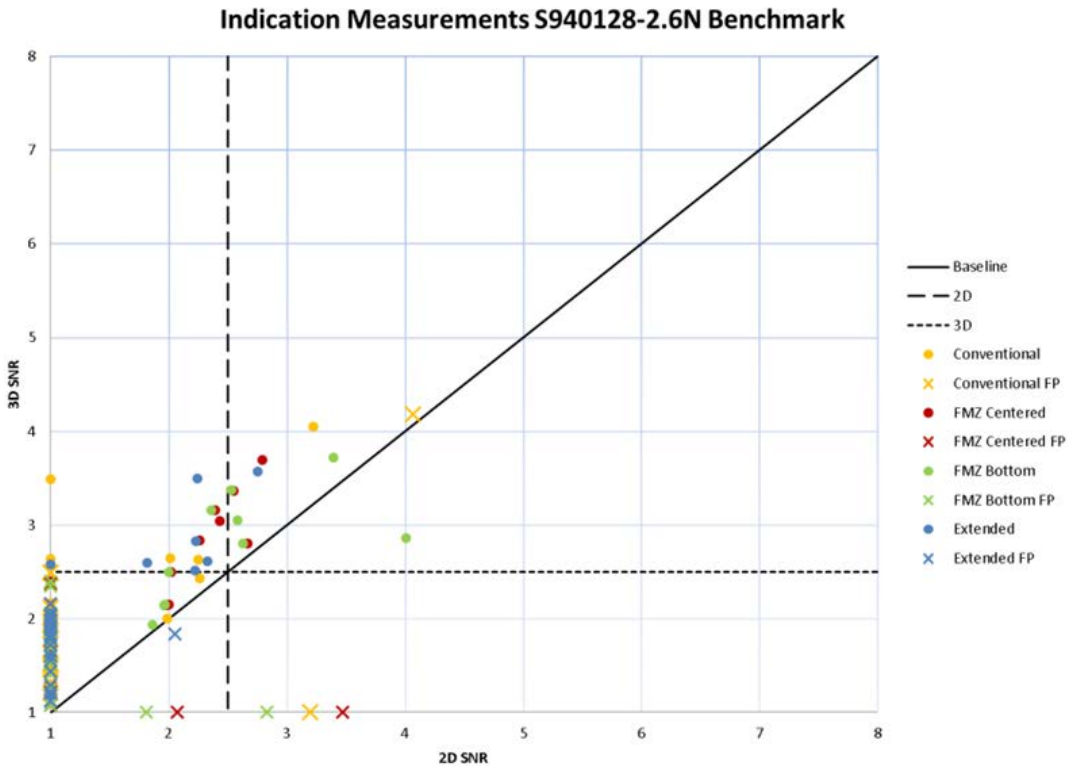

Figure 11. The 2D and 3D ADR Results for 2.6%N Ti Block

The results are also repeated for the other two inclusion Ti blocks in figures 12 and 13. While the indication SNRs for 5.2%N inclusions have shifted upward, the trends identified for the algorithms persist. The 3D ADR algorithm increases the number of detections without also increasing the number of FPs in the SA950320-5.2N block. Although the 2D ADR algorithm did detect two indications that the 3D ADR algorithm did not, these indications were of marginal strength at SNR <3, and detected many other indications that the 2D algorithm did not. Further, the 3D algorithm passed over the wide assortment of FP targets that were detected in the 2D algorithm.

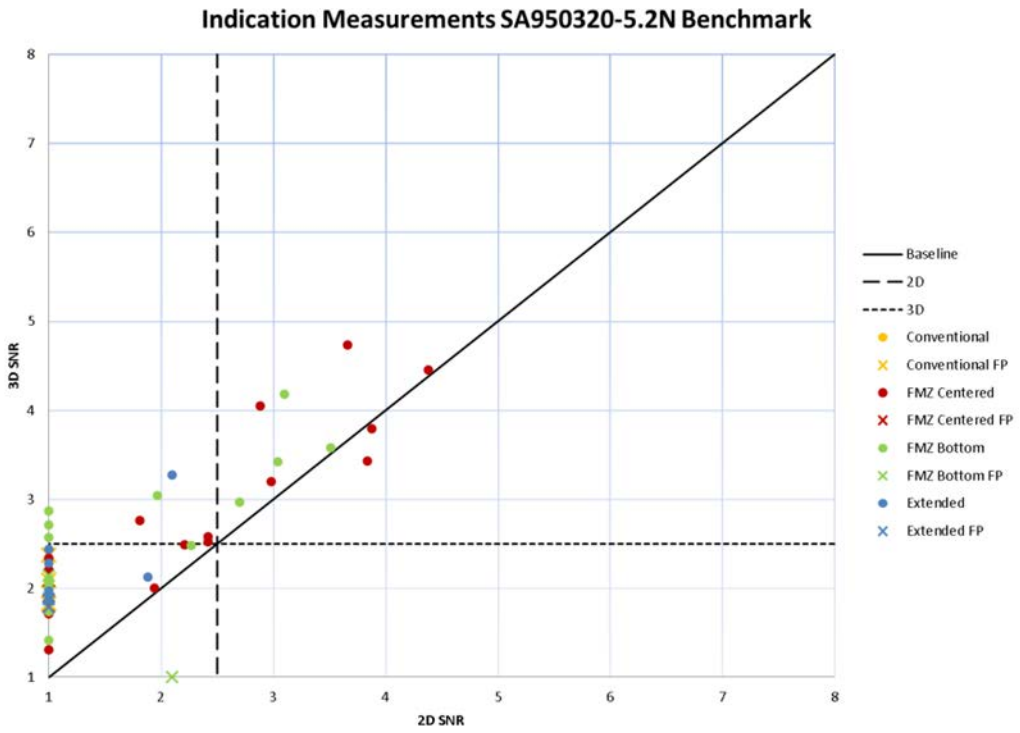

Figure 12. The 2D and 3D ADR Results for 5.2%N Ti Block

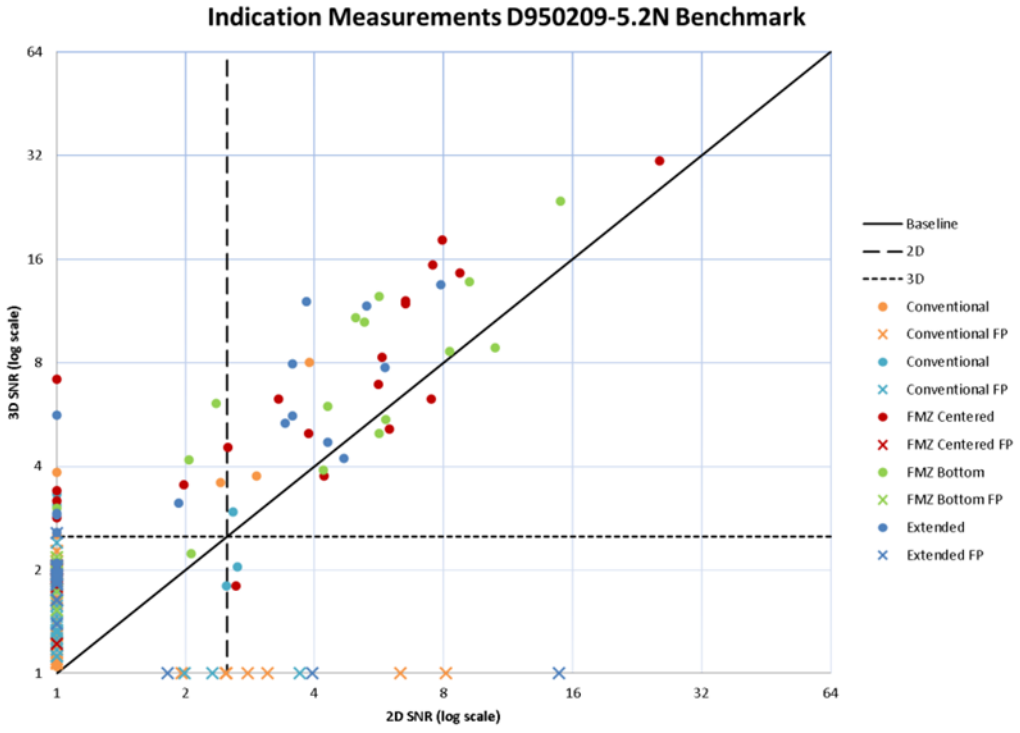

Figure 13. The 2D and 3D ADR Results for Synthetic Defect Ti Block

To summarize, for the benchmark blocks under study, the 3D ADR algorithm showed considerable improvement in the detection of the indications without a negative effect on FPR. In fact, it was shown that, at the same level of detection, FPR was improved. This can be shown another way, via analysis of the ROC curve, the parametric function describing TPR (detection) versus FPR. In this case, SNR was used as the parameter for detection for the 2D and 3D ADR algorithms.

Figure 14 shows three ROC curves for all four benchmark Ti specimens, separated in terms of the zone that was used to acquire them. These ROC curves were determined from the 2D ADR algorithm for comparison with 3D ADR. During ROC analysis, the strength of the inspection can be gauged by the area under the curve (AUC). The higher the AUC, the more TPs and fewer FPs there are. It can be observed that, as expected, the conventional zones yielded the weakest inspection, followed by the FMZ bottom, and the strongest is the entitlement scan.

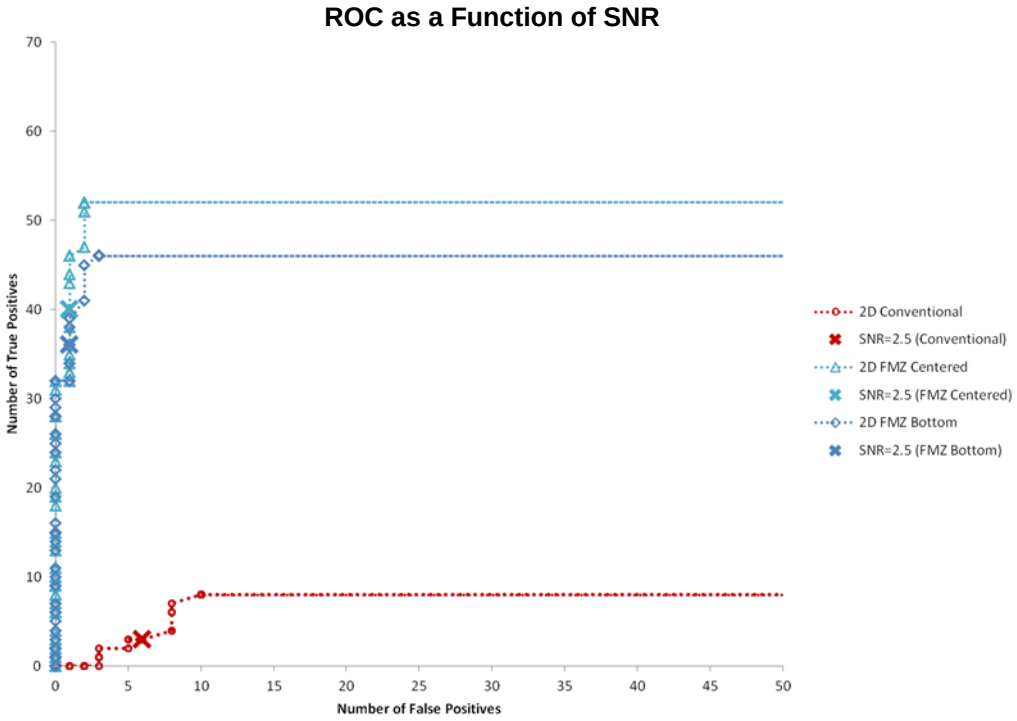

Figure 14. The ROC Curves for 2D ADR

Figure 15 shows the same ROC curves for 2D ADR, but with 3D ADR overlaid as solid lines. It can be observed with minimal inspection that the 3D ADR curves increase the AUC of their respective data sets run with 2D ADR. Furthermore, the operating point for SNR = 2.5 has been labeled on each curve. As predicted, it is observed that in each case, POD increases, while FPR decreases.

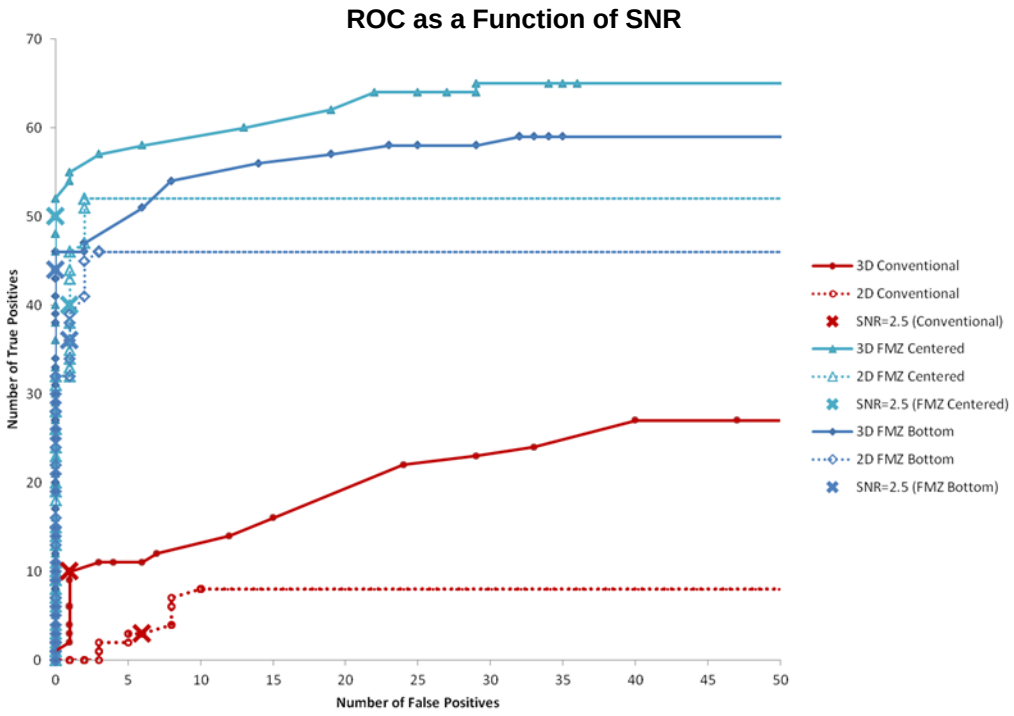

Figure 15. The ROC Curves for 2D ADR and 3D ADR Overlaid

Figure 16 shows the same 2D ROC curves, but with the extended zone under study. Because this zone is between conventional and FMZ in size, it is expected that its AUC for 2D ADR is between the conventional and FMZ result. However, it should be noted that the 3D ADR extended zone ROC curve actually has similar AUC to that of 2D ADR bottom and centered. For the most part, the curve is bounded by FMZ and entitlement. Further, the operating point is also bounded by the two. The conclusion is that the 3D ADR algorithm, when run on data from a larger zone, is comparable in performance to the 2D ADR algorithm run on data from a smaller zone. The similar detection level is expected because, as the zones decrease in size, there is more opportunity for detection and less blocking signature from background material. What is not necessarily intuitive is that increased FPR is not a penalty paid for this improvement. On the contrary, the 3D ADR algorithm increased the accuracy of the SNR as well, and was thus able to classify away the FPs that, otherwise, would have been detected.

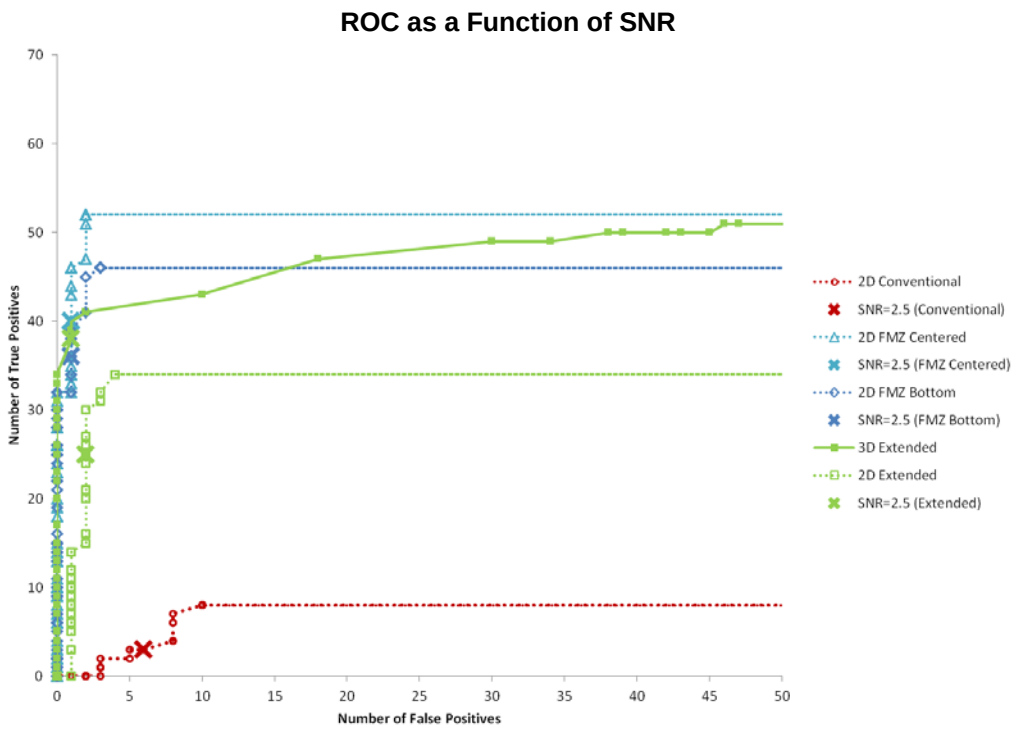

Figure 16. The ROC Curves for 2D ADR With 2D and 3D ADR Extended Zone Overlaid

6.3.2 The SID

The analyses done on the synthetic inclusion blocks were also completed for the SID in an effort to show results on a real-world application, such as a full-size disk. Gate types were varied between FMZ centered and conventional for comparison, and detection rates and FPRs were analyzed.

Figure 17 shows the results for each indication in the SID. Because many of the indications are very strong, sometimes resulting from FBHs, many of the indications are uninteresting to this study and have very large SNRs. The marginal indications appear on surfaces UH and UJ, where background signatures are higher and the indications are more difficult to detect. The plot for this case, in addition to indications and FPs, also shows the targets that are either nonrelevant or targets that would usually be detected because of SNR, geometry, and appearance, but are really nonrelevant signals, such as edge effects and air bubbles. As with the inclusion blocks, these data show that more indications are detected in the 3D ADR algorithm that were not detected in the 2D case, as well as a handful of FPs that were correctly classified in the 3D algorithm. The ROC curve for the specimen in figure 18 confirms this.

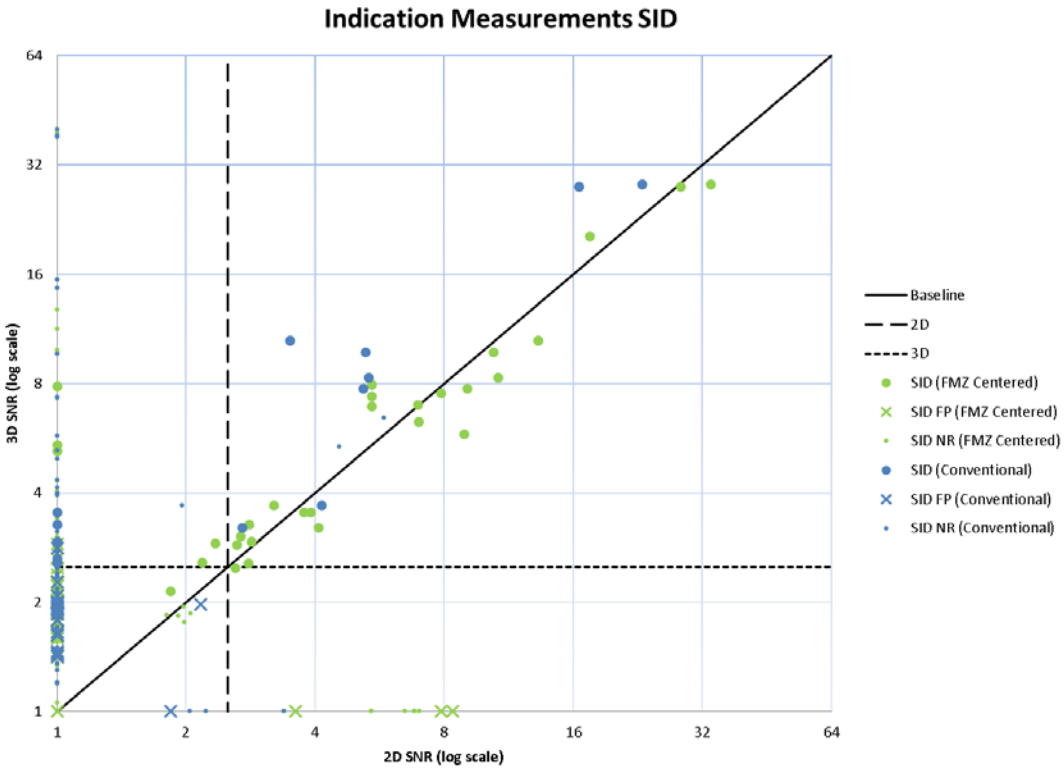

Figure 17. The 2D and 3D ADR Results for the SID

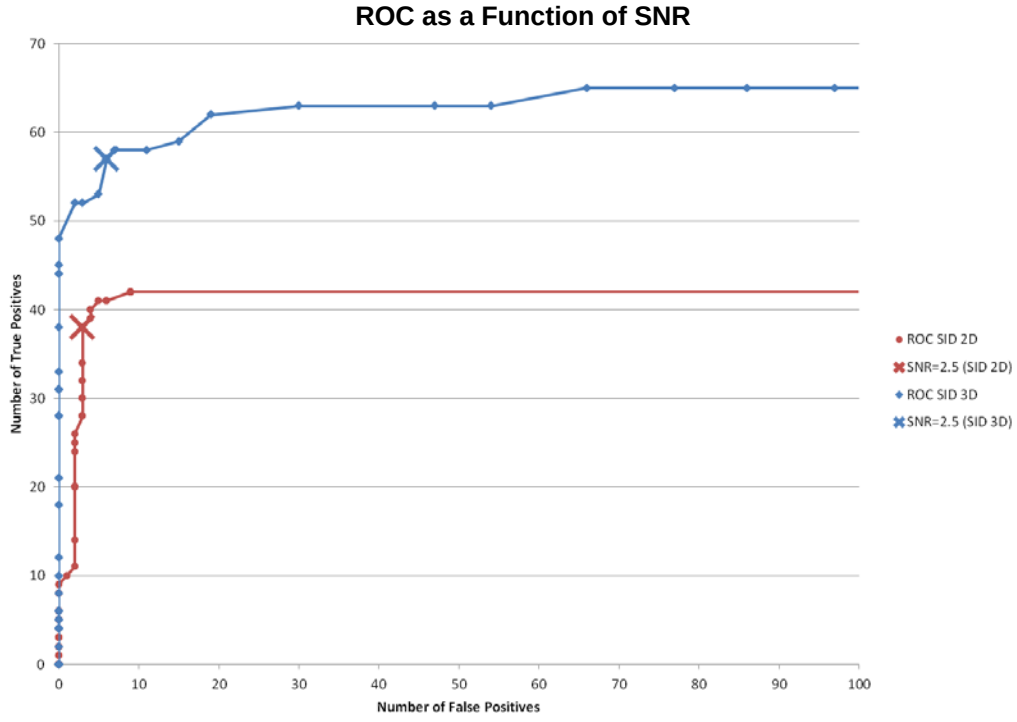

Figure 18. The ROC Curve for 2D and 3D ADR for the SID

6.3.3 Discussion

It was determined, through experimentation with conventional inspection techniques and the state-of-the-art 2D ADR algorithmic approach versus the new 3D ADR algorithmic approach, that 3D ADR significantly increases detections. However, when POD goes up, the engineer must also consider the effect on FPR. It was also observed that, compared to 2D ADR, 3D ADR effectively reduces the FPR from the microstructure.

Table 11 shows the findings in a numerical format. While the state-of-the-art 2D approach significantly increases detections and reduces FPR, its drawback is that its technique requires the more expensive FMZ approach, which increases the number of scans and the inspection time from the conventional inspection. The 3D approach significantly increases detections and further reduces the FPR from the state-of-the-art. Hence, the inspection may be allowed to increase the zone size and reduce cost and still enjoy similar statistics seen with the state-of-the-art.

Table 11. Summary of Findings for Synthetic Inclusion Blocks

Inspection Approach	Gate Setting	Detections	FPs
Conventional	Full volume	4	6
State-of-the-Art	0.5″ zones	35	2
New Approach	0.5″ zones	44	0
New Approach	1.0″ zones	38	2

This study also showed that 3D ADR provides no benefit over 2D ADR for materials with uniform microstructure, such as those based on nickel. Nickel alloys, when scanned ultrasonically, produce scans with little background signature, making them of little interest to this study. In fact, data from these specimens are generally analyzed with a very simple amplitude threshold, which is applied to the entire image and controlled through technical scan planning. The 3D ADR algorithm shows its benefits with more difficult scans to analyze—those with varying microstructure background signatures, such as Ti alloys.

Additionally, 3D ADR does not reduce FP indications due to component geometry. As seen from the SID, nonrelevant indications are still detected because the algorithm classifies on SNR and not position within the part.

ADR does produce a positive business impact. It is an enabling technology for reducing inspection cost in both the forging and billet arenas. Its improved repeatability and reproducibility over an operator-driven manual approach reduces engineering evaluation, cycle time, and uncertainty. Finally, its reliability enhances component safety and quality.

7. PRODUCTION DEMONSTRATION

The final phase of the program was the demonstration of the ADR software in an environment representative of that where forging and billet hardware are ultrasonically tested. The

production demonstration software described in section 5.2 was used for the demonstration. The component selected for the demonstration was the SID from a previous FAA program. The demonstration was held at the GE Aviation QTC in Cincinnati, Ohio. The QTC has UT equipment representative of production shops and has the capability of performing production inspections for GE Aviation when the need arises. An ultrasonic inspector qualified to level II according to the National Aerospace Standard 410 criteria performed the data collection and analysis for the demonstration. The demonstration was held February 6, 2013 and was attended by over 20 representatives from the aerospace testing and equipment industry.

7.1 TECHNICAL PLAN

The test specimen selected for the demonstration was the SID. The SID is a Ti forging that is representative of the configuration ultrasonically tested for small to mid-sized commercial aircraft engines. It has several synthetic targets inserted into the forging, including FBH and SHA seed targets, as shown in figure 19. The targets are located at several radial and circumferential locations on the disk. In total, there are more than 50 targets in the SID.

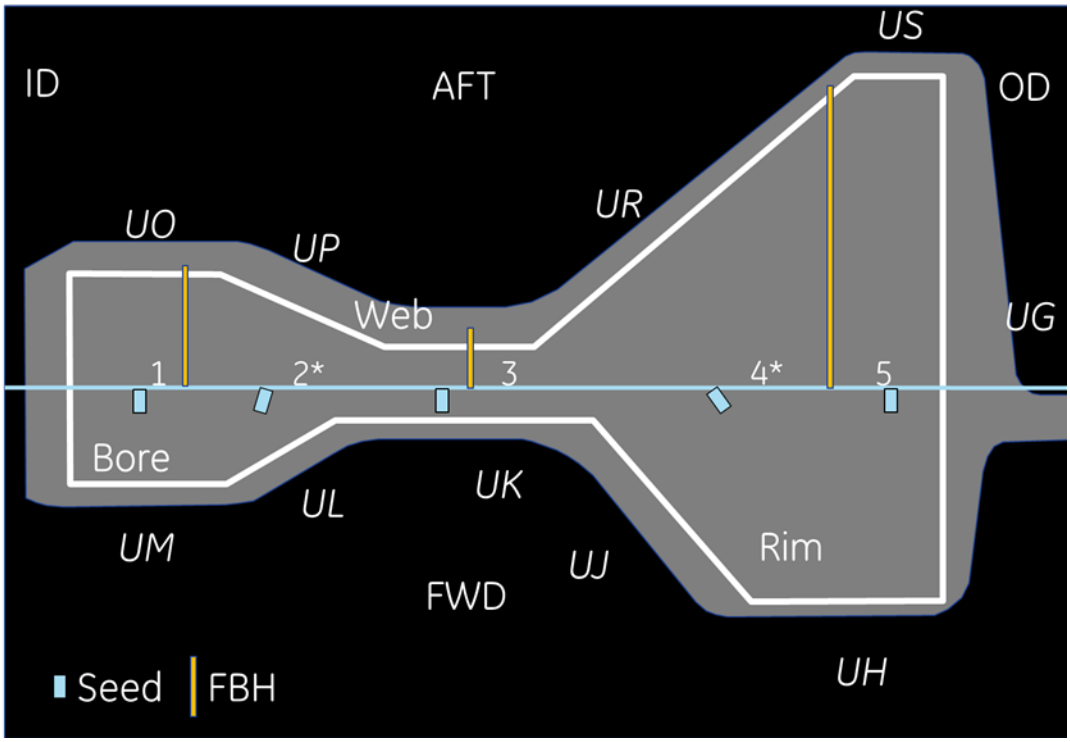

Figure 19. Diagram of the SID

An ultrasonic scan plan was developed based on the GE Aviation multizone inspection approach for forgings. Table 11 shows the zones and transducer parameters for this inspection approach. These zones were applied to the surfaces of the forging, resulting in the coverage map shown in figure 20. Tables 12 and 13 show the list of targets that will be included in the demonstration using a map of the SID.

Table 12. The FMZ Inspection Parameters

Zone	Inspection Range	Frequency	Waterpath	Diameter	Focal Length
Zone 1	0.06″ to 0.50″	10 MHz	3″	0.375″	3″
Zone 2	0.50″ to 1.00″	10 MHz	6″	1.0″	8″
Zone 3	1.00″ to 1.50″	10 MHz	4″	1.0″	8″
Zone 4	1.50″ to 2.00″	10 MHz	2″	1.0″	8″
Zone 5	2.00″ to 2.50″	10 MHz	2″	1.0″	10″

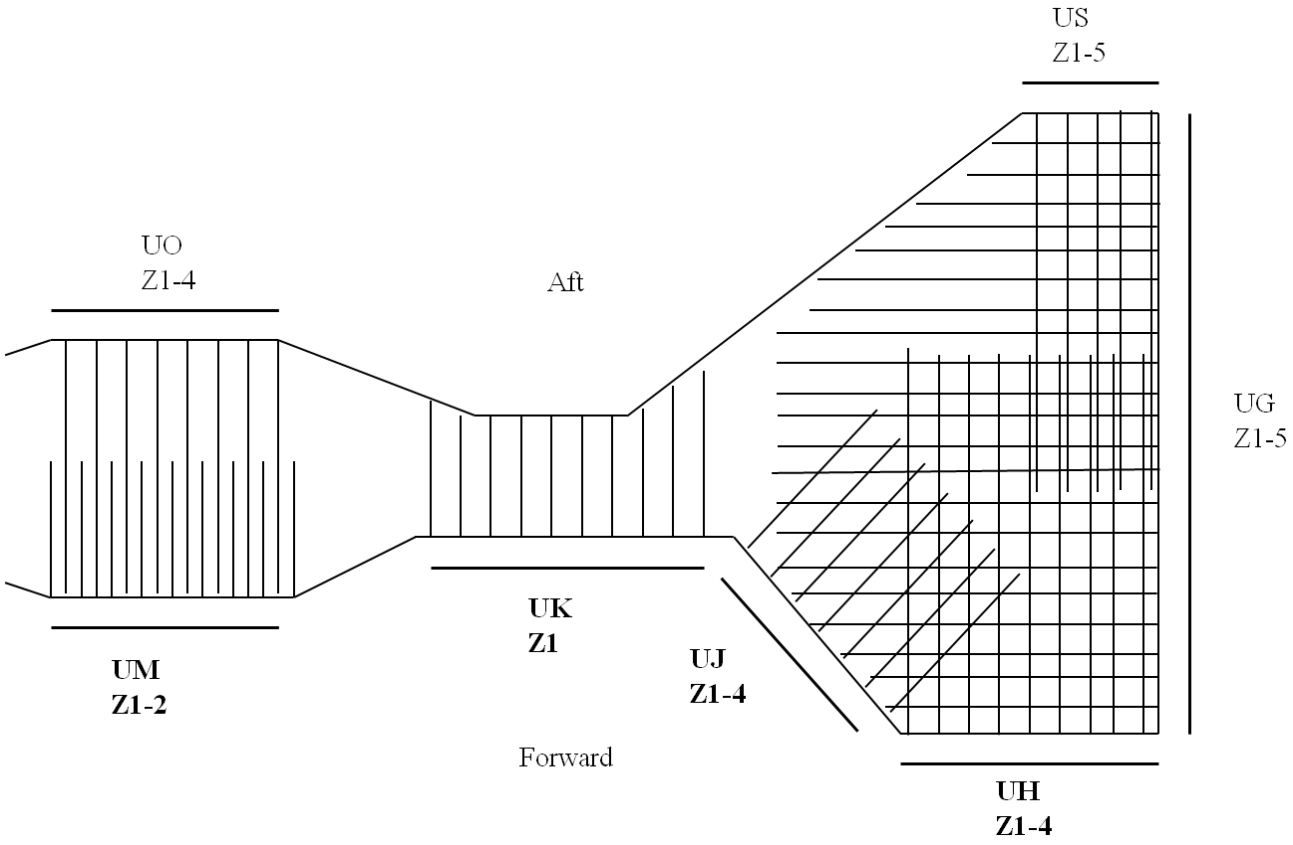

Figure 20. The SID Scan Plan

Table 13. The SID Indications for Production Demonstration

Target	Location	Size	wt%	Low Noise	High Noise
1	UG, UH	#3	3	x	
2	UH	#3	17	x	
3	UH	#3	3		x
4	UG, UH	#3	17		x
5	UG, UH	#5	3		x
6	UG, UH	#5	17		x
7	UG, UH	#5	3	x	
8	UG, UH	#5	17	x	
9	UJ	#3	3	x	
10	UJ	#3	17	x	
13	UJ	#5	3		x
14	UJ	#5	17		x
17	UK	#3	3	x	
18	UK	#3	17	x	
19	UK	#3	3		x
20	UK	#3	17		x
21	UK	#5	3	x	
22	UK	#5	17	x	
23	UK	#5	3		x
24	UK	#5	17		x
33	UM, UO	#3	3		x
34	UM, UO	#3	17		x
35	UM, UO	#3	3	x	
36	UM, UO	#3	17	x	
37	UM, UO	#5	3	x	
38	UM, UO	#5	17	x	
39	UM, UO	#5	3		x
40	UM, UO	#5	17		x

In addition to the standard zones from table 11, some zones with extended inspection ranges were selected for the demonstration. These zones will explore the ability of the 3D ADR algorithm to provide equivalent sensitivity to 2D ADR using fewer zones. Fewer zones will lead to a lower cost inspection. Table 14 lists the parameters for the extended zones.

Table 14. Extended Multizone Inspection Parameters

Zone	Inspection Range	Frequency	Waterpath	Diameter	Focal Length
Zone 1-2	0.06″ to 1.00″	10 MHz	3″	0.375″	3″
Zone 3-4	1.00″ to 2.00″	10 MHz	4″	1.0″	8″

The ultrasonic scan plan was implemented using a standard ultrasonic immersion tank that was upgraded with a waveform acquisition system from OKOS Solutions [5]. This system featured the AL12250 OKOS digitizer, which has up to a 250 MHz sampling rate with 12-bit resolution. The digitizer used a 125 MHz sampling rate for the demonstration. At 12.5 times the transducer's nominal frequency, this sampling rate was sufficient for capturing high-quality data for processing by the ADR algorithm. The mechanical system on the tank has the ability to capture data with a 0.002″ spatial resolution. Based on the nominal 0.050″ beam diameter of the transducers, a 0.020″ spatial sampling rate was selected for the demonstration.

7.2 RESULTS

On the day of the demonstration, the scan plan shown in figure 20 was implemented in the following manner. This implementation order was selected to give the best flow of events and discussion for the demonstration meeting. It was not optimized for speed or efficiency. Note that, because of time constraints, data were not collected from surfaces UG, UO, or US. Flipping the part in the ultrasonic tank is time-consuming and the data from these surfaces had no unique features when compared to the surfaces being scanned. The data were collected from the zones as shown below:

1. Data Collection of UJ Zones 1, 2, 3 and 4
2. Data Collection of UJ Zones 1-2 and 3-4
3. Data Collection of UH Zones 1, 2, 3, and 4
4. Data Collection of UH Zones 1-2 and 3-4
5. Data Collection of UK Zone 1
6. Data Collection of UM Zones 1 and 2
7. Data Collection of UM Zone 1-2

After the data were collected, they were transferred to a separate computer for the ADR analysis. This transfer was not necessary, but it freed up the data acquisition computer to gather additional data while the ADR system analyzed the data that had been collected previously. Table 15 shows the statistics from the production demonstration.

Table 15. Results From Production Demonstration

Zone	Scan Time	Scan Pixels	Index Pixels	Samples per Index	File Size (MB)
UJ 1	5.3 min	3000	88	569	244
UJ 2	5.3 min	3000	88	569	244
UJ 3	5.3 min	3000	88	569	244
UJ 4	5.3 min	3000	88	569	244
UJ 1-2	5.3 min	3000	88	1097	470
UJ 3-4	5.3 min	3000	88	1266	542
UH 1	3.7 min	3600	62	569	206
UH 2	3.7 min	3600	62	569	206
UH 3	3.7 min	3600	62	569	206
UH 4	3.7 min	3600	62	569	206
UH 1-2	3.7 min	3600	62	1097	397
UH 3-4	3.7 min	3600	62	1266	458
UK 1	4.9 min	2700	82	569	204
UM 1	3.0 min	1800	50	569	83
UM 2	3.0 min	1800	50	569	83
UM 1-2	3.0 min	1800	50	1097	160

Note that the data acquisition time listed in table 15 was not limited by the ultrasonic instrument, but rather by the mechanical system. The ultrasonic instrument has the theoretical bandwidth to collect data at greater than 20″ per second surface speed. The data analysis time listed is a composite time that includes opening the data file, rectifying the data, and performing the ADR analysis.

8. TECHNOLOGY TRANSFER

This section of the report will discuss in detail several factors that will be critical to the successful technology transfer of the 3D ADR software. These factors were identified based on the feedback of users and developers of the 2D ADR software currently used in the aerospace testing industry.

8.1 INSPECTION WORKFLOW

The seamless integration of the 3D ADR software into the workflow of the ultrasonic inspection process is the most critical factor for successful technology transfer. If the software greatly increases the cycle time for the inspection process with additional or time-consuming steps, it will not see widespread use.

To start with, the workflow of a typical inspection process used in the aerospace testing industry will be considered (shown in figure 21).

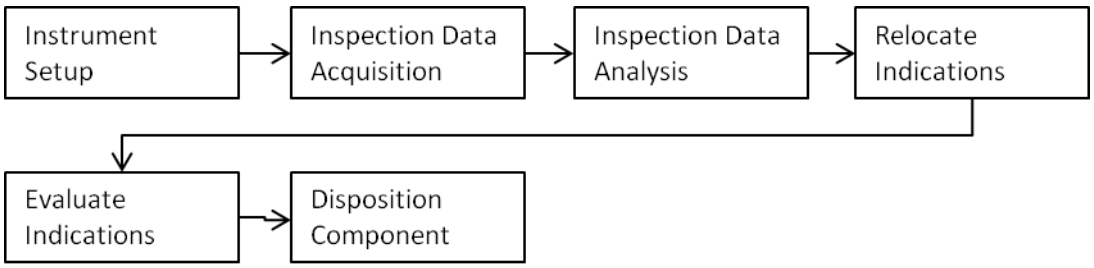

Figure 21. Typical Aerospace Inspection Workflow

In this process, the inspector sets up the inspection instrumentation, performs the inspection acquiring the data, analyzes the data after the acquisition is complete, relocates any indications identified in the analysis, and evaluates those indications per the inspection acceptance criteria. Often the evaluation process requires the inspector to move the ultrasonic transducer back to the location of the indication to complete the evaluation procedure.

The typical ultrasonic instrument used to implement this workflow uses a single personal computer (PC) to control the ultrasonic instrumentation, the mechanical system, and the data analysis. This single PC architecture allows inspection equipment vendors to provide a software solution that has access to the instrumentation setup parameters, and to position information from the motion control system and the inspection data. This architecture facilitates an efficient implementation of the workflow found in figure 21. Often, inspectors are able to reposition the mechanical system to the location where an indication occurred simply by using the PC pointing input device (mouse). On the image that contains the indication to be relocated, the operator selects the indication in the image data with the mouse. A command is then issued to the motion control software to return the mechanical scanning system to the location selected in the image.

The integration (or lack thereof) between the analysis software and the mechanical systems has a significant influence on the workflow and inspection cycle time. Figure 22 shows a scenario where ADR evaluation software is not integrated with the motion control software and additional steps are thus added to the workflow.

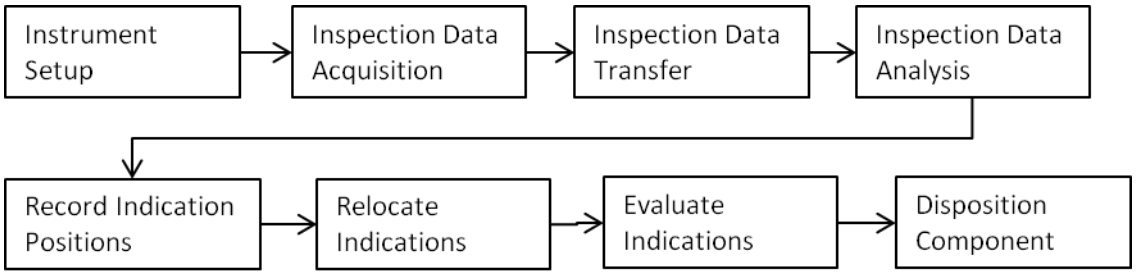

Figure 22. Inspection Workflow for Separate Motion Control and Evaluation Software

New steps are required for transferring the data to the separate evaluation software package and then transferring the position information of any indications back to the motion control software from the evaluation software package. Both of these additional steps are typically time-consuming to implement, greatly increasing inspection process cycle time.

This is only one implementation scenario for ADR evaluation software that could negatively impact inspection cycle time. Technology that increases inspection cycle time faces an uphill battle for adoption in the aerospace testing industry, which is cost-sensitive. The impact of the ADR software on the workflow shown in figure 21 is a critical factor to a successful technology transfer.

8.1.1 Inspection Cycle Time

Other factors beyond the workflow itself can impact inspection cycle time for systems using ADR evaluation software. These other factors are related to the specifics of the hardware and software used to implement the ADR system and include the speed of reading/writing the ultrasonic data from disk storage, speed of any network data transfers, efficiency of any data preprocessing software required for the ADR algorithm, and execution time of the ADR algorithm itself.

8.1.2 Data Storage and Retrieval

While waveform ultrasonic data sets provide more insight into the material being inspected, that additional insight comes with the cost of much larger data sets. The size of waveform data sets will range from 0.25 GB to 1 GB per inspection zone on a typical aerospace forging. With between 10 and 20 inspection zones per forging, 3D ultrasonic inspection methods will need to include a well thought out strategy for data management.

Fortunately, there is much that can be learned about data management from the healthcare industry, which has been dealing with large volumes of digital data for over two decades. In the late 1980s, the medical community realized the key to data management was to have a standard format for data communication and storage that included both the image data and metadata about the image. A group of industry experts created the Digital Imaging and Communications in Medicine (DICOM) standard to meet those needs. By creating a standard that encompasses both the image data and the metadata, DICOM enables the use of database technology to efficiently store and retrieve data. Two decades later, DICOM is the de facto standard used for all medical imaging applications.

In 2000, a group of nondestructive evaluation (NDE) experts sought to leverage the DICOM standard for digital inspection data. Working with the American Society for Testing and Materials (ASTM) International, the Digital Imaging and Communication in Nondestructive Evaluation (DICONDE) standard was released in 2004. By closely following the DICOM standard, DICONDE is able to leverage all the developments in the medical industry for data storage and retrieval.

8.1.3 Validation Testing

Because of the diverse nature of ultrasonic inspection applications in the aerospace industry, it is not possible to develop a one-size-fits-all ADR system. The parameters of the ADR system will need to be adjusted to accommodate the requirements of different applications. When the

parameters of the ADR system are adjusted, the performance of the ADR system will need to be determined and compared to the requirements of the application.

8.2 TECHNOLOGY TRANSFER STRATEGY

This section will discuss the recommended industry transfer approach for the technology developed in this program.

8.2.1 Overall Approach

The central tenant of the recommended technology transfer approach for this program is a flexible, open-software architecture. Such an architecture will allow the software developed to be adopted by the aerospace testing industry, improved by users with new technology, and incorporated into commercial products.

One widely used approach to creating a flexible, open-software architecture is to divide the software into different layers or tiers. This is commonly referred to as an N-tier software architecture. As the name implies, the approach is extensible to an arbitrary number of tiers, but the majority of modern software systems uses four tiers, as shown in figure 23.

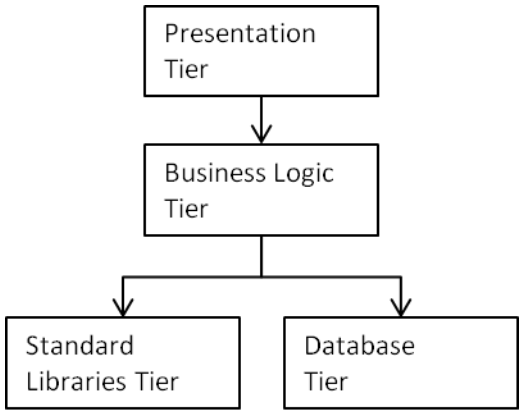

Figure 23. Typical N-Tier Software Architecture Implementation

Here, the software is logically divided between user interaction (presentation tier), application-specific computation and decisions (business logic tier), standard function calls (library tier), and data storage and retrieval (database tier).

This program implements the N-tier software architecture shown in figure 24. The core of the implementation is the ADR algorithm in the business logic layer. This ADR algorithm is accessed by a single-function call with a simple interface. The software is written in C++ using Microsoft® Visual Studio® and compiled as a DLL. This DLL can be accessed from other C++ applications or from applications developed in Java or C#.

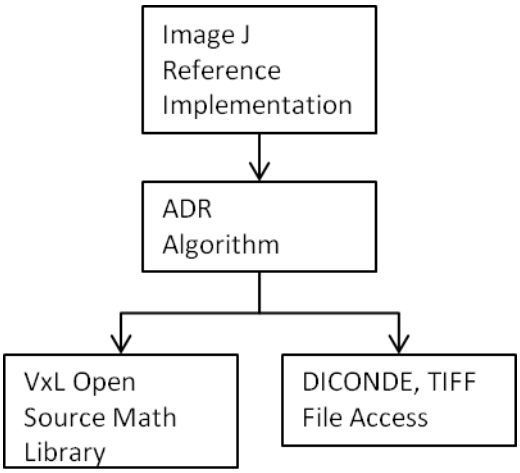

Figure 24. The 3D Ultrasonic ADR Software Implementation of N-Tier Architecture

The ADR algorithm uses the VxL open source library for standard mathematical functions needed to implement the image-processing tasks in the algorithm. Taking advantage of an open-source library for standard mathematical functions reduces the time and cost of developing the ADR software. The ADR algorithm uses a separate set of functions for accessing the data files. In addition to the proprietary file formats used on the program, access is provided to the industry standard formats of TIFF* and DICONDE.

This project provides a reference implementation using ImageJ; an open-source image analysis package created and maintained by the NIH. ImageJ is widely used to view and analyze medical and other types of image data. It is written using the Java programing language, which also serves to demonstrate that the ADR algorithm can be accessed by applications not written in C++.

This design for the ADR software will simplify the transfer of this technology. Companies wishing to use the ADR software will not be forced to access it through the ImageJ user interface. Instead, they will be able to access the ADR algorithm from their own software applications, as shown in figure 25.

This company could be an aerospace equipment manufacturer, a UT house, or an ultrasonic equipment manufacturer. This flexibility to access the ADR software in the manner shown in figure 25 addresses all of the key challenges to technology transfer described in section 8.1 of this report. The remainder of section 8.2 explains the advantages of this approach for each one of those challenges.

* TIFF stands for Tagged Image File Format

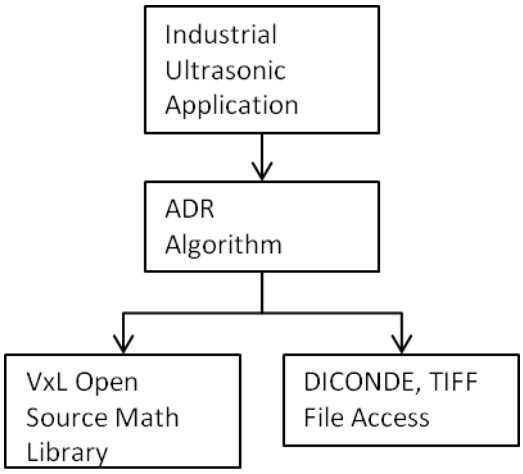

Figure 25. Example of Industry Utilization of 3D Ultrasonic ADR Software

8.2.2 Inspection Workflow

The ADR system design described above has a major advantage over standalone ADR system software with respect to inspection workflow. A standalone ADR system would require the use of the nonoptimal workflow described in figure 22. The N-tier software architecture used in this project will allow the ADR system to be implemented with the optimal workflow shown in figure 21. Ultrasonic instrument vendors will be able to incorporate the ADR algorithm into their data acquisition system software, thus eliminating the need to transfer the data to a separate computer. The integration will also allow the operators to reposition the mechanical system back at the indication directly from the ADR results because the ADR system has access to the mechanical positioning system.

8.2.3 Inspection Cycle Time

The N-tier software architecture will allow the implementer of the ADR system to optimize it for speed. There are many different technologies available for implementing computationally intensive algorithms, such as the 3D ADR algorithm. From the gaming industry, there are graphics processing units (GPU) that are designed for the rapid computations needed for 3D gaming. These units can be programmed to do rapid scientific calculations. A second technology is a field-programmable gate array (FPGA), which is an integrated circuit designed to be configured by a customer or a designer after manufacturing—hence the term "field-programmable." The FPGA configuration is generally specified using a hardware description language similar to that used for an application-specific integrated circuit (ASIC). The FPGAs can be used to implement any logical function that an ASIC could perform. A third method to consider is multithreading. Multithreading is the process of breaking code execution up into separate processes or threads that run on separate central processing units (CPU). Typical PCs have four to eight CPUs. Either of these technologies can be used separately or in combination to implement the 3D ADR algorithm in a computationally efficient manner. Such an implementation was beyond the scope of this particular program, but the N-tier architecture

allows the work of this program to be adapted to these technologies to ensure a minimum inspection cycle time from ADR system perspective.

8.2.4 Data Storage and Retrieval

The N-tier architecture allows maximum flexibility for data storage and retrieval. Because data storage and retrieval is isolated as a separate tier (as shown in figure 23), this allows the use of any data storage and retrieval method in the ADR system without having to modify the ADR algorithm. This will allow the system to be customized to use industry-standard DICONDE tools or speed-optimized proprietary solutions.

8.2.5 Validation Testing

Validation testing is simplified also by the use of the N-tier architecture. Because the presentation tier can be changed without impacting the ADR algorithm, different presentation tiers can be designed to simplify validation testing. For example, a specific presentation layer can be created for easily adjusting ADR parameters and rapidly seeing the impacts of the changes. A separate presentation layer could be created to process the results of ADR validation testing to automatically produce receiver operating characteristic (ROC) curves for the ADR system. Such custom presentation layers can greatly reduce the cycle time and the cost of ADR system development and validation.

Finally, the company implementing the ADR system will have access to the source code for the ADR algorithm. Typically, the validation of the algorithm will result in the need to adjust the algorithm. For most cases, this should be accomplished using the ADR algorithm parameters. In some cases, though, adjusting the parameters may not be enough to achieve the desired performance. In such cases, the company implementing the ADR system will have the opportunity to modify the source code of the algorithm to improve it and obtain the desired performance for the application.

8.3 INDUSTRY FEEDBACK

Industry feedback on this recommended technology transfer approach was solicited on two occasions. Two virtual meetings were held with industry experts using teleconference and web meeting technology. The first meeting was held on August 15, 2012. This meeting was attended by the people listed in table 16.

Table 16. Attendees of August 15, 2012 Virtual Technology Transfer Meeting

Attendee	Company
Geoff Schotts	OKOS
Andre Maitre	GE Measurement and Control
Michael Schnee	GE Measurement and Control
Norbert Steinhoff	GE Measurement and Control
Pat Howard	GE Aviation
Andy Ferro	GE Aviation

During the meeting, the participants verified that the N-tier architecture described in this document would allow the companies to incorporate the ADR algorithm into their software products. They noted that this approach would allow the software to be used on a GPU platform. This valuable feedback was incorporated into the technology transfer plan. Participants noted they experienced technical issues when using ImageJ as a presentation layer. GE Aviation was experiencing similar technical issues with the use of ImageJ; some that were overcome during the course of the project and some that were not.

A second technology transfer meeting was held on August 17, 2012 using the same format as in the previous meeting. The attendees of that meeting are listed in table 17.

Table 17. Attendees of August 17, 2012 Virtual Technology Transfer Meeting

Attendee	Company
Ken Bishop	Matec
Eric Pierce	Matec
Jim Naquin	Scanmaster
Norbert Steinhoff	GE Measurement and Control
Pat Howard	GE Aviation
Andy Ferro	GE Aviation

The outcome of the second meeting confirmed the outcome of the first meeting.

9. RECOMMENDATIONS

Based on the lessons learned during the program and input from the TWG, the team has the following recommendations for follow-on work:

- The rectification of the data as a preprocessing step for the ADR algorithm was implemented using standard programming techniques as part of the ADR software. This operation should be moved forward in the data acquisition system. The OKOS system has the ability to do that, using FPGA technology.

- The ADR algorithm that was developed did not demonstrate the ability to reduce FPs resulting from component geometry. The algorithm can be improved by introducing a model for reducing FPs from component geometry.

- The 3D ADR algorithm should be migrated to high-speed programming techniques based on the use of GPUs and multithreading.

- The mechanical system at QTC was not able to test the speed limits of the OKOS data acquisition system. Verification of 3D data acquisition and higher speeds should be performed.

- The use of 3D data acquisition will produce large volumes of data that need to be archived. The adoption of a data storage standard that includes both data and rich metadata that are searchable is essential to managing the data. The ASTM International Standard E2339 DICONDE is one such standard.

- The implementation of ADR algorithms is a relatively immature technology in the NDE industry. As a result, there is a lot of variation in the approach to validating the algorithms for use in an industrial setting. An industry standard for validation of ADR algorithms should be created. This standard should cover validation testing methodology and validation sample sizes and will greatly increase the number of ADR algorithms implemented into the production environment.

10. CONCLUSION

This program set out to investigate the potential advantages for detection of material anomalies by using three-dimensional (3D) ultrasonic data instead of the traditional two-dimensional (2D) C-scan images. Toward that end, a set of test specimens of different aerospace alloys with real and artificial anomalies was defined. Ultrasonic waveform data were collected on those test specimens to create a set of test images with a broad cross-section of signal-to-noise ratio.

Using the set of test images, an assisted defect recognition (ADR) algorithm prototype was developed that used the 3D ultrasonic data. This algorithm was tested extensively using the broad cross-section of images and compared to the results of the state-of-the-art 2D ADR techniques. This testing showed three clear advantages of using 3D ADR. First, the 3D algorithm demonstrated improved detection of the material anomalies when compared to the 2D algorithm. In particular, several synthetic hard alpha targets with low reflectivity that were not

detected with the 2D ADR approach were detected using 3D ADR. Second, 3D ADR reduced false positive (FP) inspection results due to titanium (Ti) microstructure. The FPs increase the cost of ultrasonic inspection by causing the unnecessary scrapping of good material. The third advantage of 3D ADR was that larger volumes of material could be inspected while maintaining the same sensitivity as 2D ADR. This advantage could result in a productivity improvement for the inspection of aerospace billet and forgings.

The prototype 3D ADR algorithm was ported to a C++ library suitable for industrial implementation. A test harness for the C++ library was written in Java using the open-source ImageJ platform. Writing the industrial version of the software as a multitiered application enables easy reuse of the software by ultrasonic equipment vendors. The industrial software had an execution time of nine minutes for data files collected from a typical aerospace forging. There is room to reduce this execution time by porting the C++ library to a low-cost, high-speed computing platform using graphics processing units or field-programmable gate array. Implementation on a high-speed computing platform was beyond the scope of this program.

Finally, a demonstration of the 3D ADR technology was held in an environment representative of production ultrasonic inspection for aerospace forgings. Using a commercial off-the-shelf 3D ultrasonic data acquisition system from OKOS Systems, a small Ti forging with synthetic targets was scanned by a National Aerospace Standard 401 certified level II operator. Full 3D ultrasonic data were collected at over 20″ per second surface speed. The speed was limited to 20″ per second by the performance of the mechanical system. To the surprise of the project team, the ultrasonic data acquisition system was not limiting the data acquisition speed and could support higher speeds than those demonstrated. The level II operator analyzed the data using 3D ADR industrial software. The 3D algorithm demonstrated the improved results over the 2D algorithm in this production-representative environment.

11. REFERENCES

1. L. Brasche et al., “Contaminated Billet Study,” Report DOT/FAA/AR-05/16, Federal Aviation Administration, September, 2005.

2. R.B. Thompson et al., “Engine Titanium Consortium Phase 1,” Federal Aviation Administration Report, Grant Number 94-G-048, September, 1995.

3. Exelis Visual Information Solutions, www.exelisvis.com

4. ImageJ, http://rsbweb.nih.gov/ij

5. OKOS, www.okos.com

6. Ferro, F. and Howard, P. J., “Assisted Defect Recognition for the Ultrasonic Multizone Inspection of Titanium Forgings,” Quantitative Nondestruction Evaluation: Proceedings of the 35th Annual Review of Progress in Quantitative Nondestruction Evaluation, Chicago, Illinois, July 20-25, 2008.

7. Howard, P.J., Copley, D.C., and Gilmore, R.S., “The Application of a Dynamic Threshold to C-Scan Images with Variable Noise,” *Quantitative Nondestruction Evaluation*, 1998, pp. 2013-2019.

APPENDIX A—ULTRASONIC DATA FILL

Specimen Name	File Name	Material	Scan Spacing (in)	Index Spacing (in)	Sample Rate (samp/ms)	Sample Size (in/samp)	F/#	Probe Freq. (Hz)	Probe Diam. (")	Water Path (")	SNR Level	Noise Pattern	Edge Target?
HL11-P60	HL11-P60.rf	Ni	0.01	0.01	100	0.0019		10000000			High	Low, Uniform	
HL11-P148	HL11-P148.rf	Ni	0.01	0.01	100	0.0019		10000000			High	Low, Uniform	
HL11-I148	HL11-I148.rf	Ni	0.01	0.01	100	0.0019		10000000			Low	Low, Uniform	
HL11-I60	HL11-I60.rf	Ni	0.01	0.01	100	0.0019		10000000			High	Low, Uniform	
CBGAKB30	CBGAKB30.rf	Ti	0.01	0.01	100	0.0020		10000000			High	Low	
Billet 1 Ind. 2	B1I2I7.RF	Ti	0.02	0.02	50	0.0040	8	5000000	0.75	6.1	high		
Billet 2 Ind. 1	B2I1I7.RF	Ti	0.02	0.02	50	0.0040	8	5000000	0.75	6.1			
Billet 2 Ind. 2	B2I2I7_3.RF	Ti	0.02	0.02	50	0.0040	8	5000000	0.75	6.1			
Billet 2 Ind. 2	B2I2Z2RF.RF	Ti	0.02	0.02	50	0.0040	8	5000000	1	3.0	high	low	
Billet 2 Ind. 3	B2I3I7R1.RF	Ti	0.02	0.02	50	0.0040	8	5000000	0.75	6.1	low		
Billet 2 Ind. 3	B2I3I7R2.RF	Ti	0.02	0.02	50	0.0040	8	5000000	0.75	6.1	med		
Billet 2 Ind. 3	B2I3I7R3.RF	Ti	0.02	0.02	50	0.0040	8	5000000	0.75	6.1	med		
Billet 2 Ind. 3	B2I3I7R4.RF	Ti	0.02	0.02	50	0.0040	8	5000000	0.75	6.1	med		
Billet 2 Ind. 3	B2I3I7R5.RF	Ti	0.02	0.02	50	0.0040	8	5000000	0.75	6.1	high		
Billet 3 Ind. 1	B3I1I7.RF	Ti	0.02	0.02	50	0.0040	8	5000000	0.75	6.1	high		
CDY257	CDY2f6.RF	Ti	0.02	0.02	100	0.0020	6	10000000	1	1.8	none		
CDY162	CDYF6.RF	Ti	0.02	0.02	100	0.0020	6	10000000	1	0.6	med		
CDY162	CDYI3.RF	Ti	0.02	0.02	100	0.0020	8	10000000	0.43	0.7	med	high variable	X
SID UGH H6, H5, H4	SIDUGH6A.RF	Ti	0.02	0.02	100	0.0020	6	10000000	1	3.8	low		X
SID UGH H6, H5, H4	SIDUGH6B.RF	Ti	0.02	0.02	100	0.0020	6	10000000	1	3.8	low/high	med variable	X
SID UGH H8, H7, J6, J5	SIDUGH8.RF	Ti	0.02	0.02	100	0.0020	5	10000000	0.375	2.1			
SID UGH H8, H7, J6, J5	SIDUGH8A.RF	Ti	0.02	0.02	100	0.0020	6	10000000	1	0.8	low		X
SID UGH H8, H7, J6, J5	SIDUGH8B.RF	Ti	0.02	0.02	100	0.0020	6	10000000	1	3.8	low		X
SID UH H3-H6	SIDUHZ1A.RF	Ti	0.02	0.02	100	0.0020	8	10000000	0.43	3.0	low	low	
SID UH R3-R4	SIDUHZ1B.RF	Ti	0.02	0.02	100	0.0020	8	10000000	0.43	3.0	low	low	
SID UH H1-H2, J1-J2	SIDUHZ1D.RF	Ti	0.02	0.02	100	0.0020	8	10000000	0.43	3.0	low	low	
SID UH R7-R8	SIDUHZ1E.RF	Ti	0.02	0.02	100	0.0020	8	10000000	0.43	3.0	low	low	
SID UH H7-H8, J5-J6	SIDUHZ1F.RF	Ti	0.02	0.02	100	0.0020	8	10000000	0.43	3.0	low	low	
SID UH H3-H6	SIDUHZ4A.RF	Ti	0.02	0.02	100	0.0020	6	10000000	1	0.8	med	low	
SID UH R3-R4	SIDUHZ4B.RF	Ti	0.02	0.02	100	0.0020	6	10000000	1	0.8	med	low	
SID UH none	SIDUHZ4C.RF	Ti	0.02	0.02	100	0.0020	6	10000000	1	0.8	med	low	
SID UH H1-H2, J1-J2	SIDUHZ4D.RF	Ti	0.02	0.02	100	0.0020	6	10000000	1	0.8	med	low	
SID UH R7-R8	SIDUHZ4E.RF	Ti	0.02	0.02	100	0.0020	6	10000000	1	0.8	med	low	
SID UH H7-H8, J5-J6	SIDUHZ4F.RF	Ti	0.02	0.02	100	0.0020	6	10000000	1	0.8	med	low	
SID UK K3, K4	SIDUKK3A.RF	Ti	0.02	0.02	100	0.0020	5	10000000	0.375	1.4	high	low	
F950508-1.5L	FAABlock1_I3_pt5inWP_Scout_ph01_asc2.acq	Ti	0.01	0.01	100	0.0020	8	10000000	0.375	0.5	Medium	High, uniform	
F950508-1.5L	FAABlock1_I3_2inWP_Scout_ph01_asc2.acq	Ti	0.01	0.01	100	0.0020	8	10000000	0.375	2.0	Low	High, uniform	
F950508-1.5L	FAABlock1_10f6_1pt5inWP_ph01_asc2.acq	Ti	0.01	0.01	100	0.0020	6	10000000	1	1.5	High	High, uniform	
F931213-2.5L	FAABlock2_10f10_2inWP_ph01_asc2.acq	Ti	0.01	0.01	100	0.0020	10	10000000	1	2.0	High	Low, variable	
F931213-2.5L	FAABlock2_10f10_5inWP_ph01_asc2.acq	Ti	0.01	0.01	100	0.0020	10	10000000	1	5.0	Medium	High, variable	
F931213-2.5L	FAABlock2_I3_1inWP_plus6dB_ph01_asc2.acq	Ti	0.01	0.01	100	0.0020	8	10000000	0.375	1.0	Low	High, variable	
AF3	BlockAF3_I3_3inWP_B_ph01_asc2.acq	Ni	0.01	0.01	100	0.0019	8	10000000	0.375	3.0	High	Low, Uniform	
AF13	BlockAF13_I3_3inWP_A_ph01_asc2.acq	Ni	0.01	0.01	100	0.0019	8	10000000	0.375	3.0	Medium	High, variable	
AF13	BlockAF13_5f6_3inWP_A_ph01_asc2.acq	Ni	0.01	0.01	100	0.0019	6	5000000	0.5	3.0	Low	High, variable	
AB198	BlockAB198_I3_3inWP_ph01_asc2.acq	Ni	0.01	0.01	100	0.0019	8	10000000	0.375	3.0	None	Low	
AF2	BlockAF2_I3_3inWP_b_ph01_asc2.acq	Ni	0.01	0.01	100	0.0019	8	10000000	0.375	3.0	High	Spotty	
F950508-2.5L	F950508_25L_10f10_2inWP	Ti17	0.01	0.01	100	0.0020	10	10000000	1	2.0	High	uniform	
F950508-2.5L	F950508_25L_10f10_5inWP	Ti17	0.01	0.01	100	0.0020	10	10000000	1	5.0	Medium	uniform	
F950508-2.5L	F950508_25L_10f10_3pt5inWP	Ti17	0.01	0.01	100	0.0020	10	10000000	1	3.5	Low	uniform	
F950508-2.5L	F950508_25L_10f10_2pt75inWP	Ti17	0.01	0.01	100	0.0020	10	10000000	1	2.8	Medium	uniform	
S950320-5.2N	S950320_52N_10f10_2inWP	Ti17	0.01	0.01	100	0.0020	10	10000000	1	2.0	Medium		
S950320-5.2N	S950320_52N_10f10_2inWP_B	Ti17	0.01	0.01	100	0.0020	10	10000000	1	2.0	medium	uniform	
S950320-5.2N	S950320_52N_10f10_4pt5inWP	Ti17	0.01	0.01	100	0.0020	10	10000000	1	4.5	n/a		
S950320-5.2N	S950320_52N_10f10_4inWP	Ti17	0.01	0.01	100	0.0020	10	10000000	1	4.0	n/a		
S950320-5.2N	S950320_52N_10f10_3inWP	Ti17	0.01	0.01	100	0.0020	10	10000000	1	3.0	low (?)		
S950320-5.2N	S950320_52N_10f10_2pt5inWP	Ti17	0.01	0.01	100	0.0020	10	10000000	1	2.5	low/medium		
F931213-1.5L	F931213_1.5L_3inWP (I3 transducer)	Ti64	0.01	0.01	100	0.0020	8	10000000	0.375	3.0	high	uniform	
F931213-1.5L	F931213_1.5L_I3_3inWP_B	Ti64	0.01	0.01	100	0.0020	8	10000000	0.375	3.0	high	uniform	
F931213-1.5L	F931213_1.5L_I3_1inWP	Ti64	0.01	0.01	100	0.0020	8	10000000	0.375	1.0	high	uniform	
F931213-1.5L	F931213_1.5L_I3_3inWP_2degIncident	Ti64	0.01	0.01	100	0.0020	8	10000000	0.375	3.0	high	uniform	
F931213-1.5L	F931213_1.5L_I3_3inWP_3degIncident	Ti64	0.01	0.01	100	0.0020	8	10000000	0.375	3.0	high	uniform	
F931213-1.5L	F931213_1.5L_I3_3inWP_5degIncident	Ti64	0.01	0.01	100	0.0020	8	10000000	0.375	3.0	high-med	uniform	
F931213-1.5L	F931213_1.5L_I3_3inWP_6degIncident	Ti64	0.01	0.01	100	0.0020	8	10000000	0.375	3.0	Medium	uniform	
D950209_5.2N	D950209_52N_10f10_2inWP	Ti64	0.01	0.01	100	0.0020	10	10000000	1	2.0			
D950209_5.2N	D950209_52N_10f10_2inWP_B	Ti64	0.01	0.01	100	0.0020	10	10000000	1	2.0	High	uniform	
D950209_5.2N	D950209_52N_10f6_2inWP	Ti64	0.01	0.01	100	0.0020	6	10000000	1	2.0	n/a		
D950209_5.2N	D950209_52N_10f6_1_5inWP	Ti64	0.01	0.01	100	0.0020	6	10000000	1	1.5			
D950209_5.2N	D950209_52N_10f6_1inWP	Ti64	0.01	0.01	100	0.0020	6	10000000	1	1.0	low (spherical)		
D950209_5.2N	D950209_52N_10f6_1inWP_B	Ti64	0.01	0.01	100	0.0020	6	10000000	1	1.0	low/medium		
D950209_5.2N	D950209_52N_10f6_1inWP_C	Ti64	0.01	0.01	100	0.0020	6	10000000	1	1.0	saturation		
D950209_5.2N	D950209_52N_10f6_1inWP_5degIncident	Ti64	0.01	0.01	100	0.0020	6	10000000	1	1.0	still saturated		
F950508-1.5S	F950508-15S_5F8_6inWP_45degLwave	Ti17	0.01	0.01	100	0.0020	8	5000000	0.75	6.0	~medium on 1's		
F950508-1.5S	F950508-15S_5F8_6inWP_45degLwave_B	Ti17	0.01	0.01	100	0.0020	8	5000000	0.75	6.0	low		
F950508-1.5S	F950508-15S_5F8_6inWP_45degLwave_C	Ti17	0.01	0.01	100	0.0020	8	5000000	0.75	6.0	medium	uniform	
S940128-2.6N	S940128_26N_10f10_2inWP	Ti64	0.01	0.01	100	0.0020	10	10000000	1	2.0	n/a		
S940128-2.6N	S940128_26N_10f6_2inWP	Ti64	0.01	0.01	100	0.0020	6	10000000	1	2.0	n/a		
S940128-2.6N	S940128_26N_10f6_2_6inWP	Ti64	0.01	0.01	100	0.0020	6	10000000	1	2.6	n/a		
S940128-2.6N	S940128_26N_10f6_2_6inWP_B	Ti64	0.01	0.01	100	0.0020	6	10000000	1	2.6	n/a		
S940128-2.6N	S940128_26N_10f6_2_6inWP_C	Ti64	0.01	0.01	100	0.0020	6	10000000	1	2.6	medium/high	variable	
S940128-2.6N	S940128_26N_10f6_3_5inWP	Ti64	0.01	0.01	100	0.0020	6	10000000	1	3.5	n/a		
S940128-2.6N	S940128_26N_10f6_3inWP	Ti64	0.01	0.01	100	0.0020	6	10000000	1	3.0	n/a		
S940128-2.6N	S940128_26N_10f6_3inWP_B	Ti64	0.01	0.01	100	0.0020	6	10000000	1	3.0	low		
S940128-2.6N	S940128_26N_10f6_3inWP_C	Ti64	0.01	0.01	100	0.0020	6	10000000	1	2.8	medium/low		
S940119-1.6N	S940119_16N_10f6_2_8inWP	Ti64	0.01	0.01	100	0.0020	6	10000000	1	2.8	n/a	spotty	
S940119-1.6N	S940119_16N_10f6_2_6inWP	Ti64	0.01	0.01	100	0.0020	6	10000000	1	2.6	low	spotty	
S940119-1.6N	S940119_16N_10f6_2_4inWP	Ti64	0.01	0.01	100	0.0020	6	10000000	1	2.4	low	spotty	
S940119-1.6N	S940119_16N_10f6_2inWP	Ti64	0.01	0.01	100	0.0020	6	10000000	1	2.0	low	spotty	
S940119-1.6N	S940119_16N_10f6_1_8inWP	Ti64	0.01	0.01	100	0.0020	6	10000000	1	1.8	high	spotty	
S940119-1.6N	S940119_16N_10f6_1_8inWP_B	Ti65	0.01	0.01	100	0.0020	6	10000000	1	1.8	high	spotty	
S940119-1.6N	S940119_16N_10f6_1_8inWP_C	Ti65	0.01	0.01	100	0.0020	6	10000000	1	1.8	medium	spotty	

Figure A-1. Ultrasonic Data Fill

Specimen Name	File Name	Material	Scan Spacing (in)	Index Spacing (in)	Sample Rate (samp/ms)	Sample Size (in/samp)	F/#	Probe Freq. (Hz)	Probe Diam. (")	Water Path (")	SNR Level	Noise Pattern	Edge Target?	
S940217-5.9N	S940217_59N_10f6_1_8inWP	Ti65	0.01	0.01	100	0.0020	6	10000000	1	1.8	high	uniform		
S940217-5.9N	S940217_59N_10f6_1_8inWP_B	Ti65	0.01	0.01	100	0.0020	6	10000000	1	1.8	high	uniform		
S940217-5.9N	S940217_59N_10f6_3inWP	Ti65	0.01	0.01	100	0.0020	6	10000000	1	3	low/medium/high	uniform		
S941202-2.8N	S941202_28N_10f6_1_8inWP	Ti17	0.01	0.01	100	0.0020	6	10000000	1	1.8	medium-high	uniform		
S941202-2.8N	S941202_28N_10f6_1_8inWP_B	Ti17	0.01	0.01	100	0.0020	6	10000000	1	1.8	medium	uniform		
S941202-2.8N	S941202_28N_10f6_3inWP	Ti17	0.01	0.01	100	0.0020	6	10000000	1	3.0	low	uniform		
S941202-2.8N	S941202_28N_10f6_2_6inWP	Ti17	0.01	0.01	100	0.0020	6	10000000	1	2.6	low	uniform		
S941202-2.8N	S941202_28N_10f10_3_2inWP	Ti17	0.01	0.01	100	0.0020	10	10000000	1	3.2	low	uniform		
F950508_2.5S	F950508_25S_10f6_6inWP_B	Ti17	0.01	0.01	100	0.0020	10	10000000	1	6.0	unsure	uniform		
F950508_2.5S	F950508_25S_10f6_6inWP_C	Ti17	0.01	0.01	100	0.0020	10	10000000	1	6.0	low-medium	uniform		
F950508_2.5S	F950508_25S_10f6_6inWP_D	Ti17	0.01	0.01	100	0.0020	10	10000000	1	6.0	none	striped		
CBGRF076	CBGRF076_20f325_1pt3inWP	Ti17	0.01	0.01	100	0.0020	3.25	15000000	0.4	1.3	n/a			
CBGRF076	CBGRF076_20f325_1pt3inWP_B	Ti17	0.01	0.01	100	0.0020	3.25	15000000	0.4	1.3	n/a			
CBGRF076	CBGRF076_20f325_pt9inWP	Ti17	0.01	0.01	100	0.0020	3.25	15000000	0.4	0.9	n/a			
CBGRF076	CBGRF076_20f325_2pt7inWP	Ti17	0.01	0.01	100	0.0020	3.25	15000000	0.4	2.7	high	uniform		
CBGRF076	CBGRF076_20f325_1pt5inWP	Ti17	0.01	0.01	100	0.0020	3.25	15000000	0.4	1.5	medium			
CBGRF076	CBGRF076_10f6_2inWP	Ti17	0.01	0.01	100	0.0020	6	10000000	1	2.0	n/a			
CBGRF076	CBGRF076_10f6_4inWP	Ti17	0.01	0.01	100	0.0020	6	10000000	1	4.0	n/a			
CBGRF076	CBGRF076_10f8_2pt5inWP	Ti17	0.01	0.01	100	0.0020	8	10000000	0.375	2.5	very low			
CBGRF076	CBGRF076_10f8_2pt5inWP_B	Ti17	0.01	0.01	100	0.0020	8	10000000	0.375	2.5	low/medium?	?		
CBGRF076	CBGRF076_10f8_2pt5inWP_C	Ti17	0.01	0.01	100	0.0020	8	10000000	0.375	2.5	low/medium?	variable		
CBGRF076	CBGRF076_10f8_2pt5inWP_D	Ti17	0.01	0.01	100	0.0020	8	10000000	0.375	2.5	low			
S940128-2.6N	S940128_26N_10_Gilmore_1pt1inWP	Ti64	0.01	0.01	100	0.0020		10000000	2	1.1	n/a			
S940128-2.6N	S940128_26N_10_Gilmore_1pt1inWP_B	Ti64	0.01	0.01	100	0.0020		10000000	2	1.1				
S940128-2.6N	S940128_26N_10_Gilmore_1pt25inWP	Ti64	0.01	0.01	100	0.0020		10000000	2	1.3	medium	variable		
S940128-2.6N	S940128_26N_10_Gilmore_1pt45inWP	Ti64	0.01	0.01	100	0.0020		10000000	2	1.5	low			
S940128-2.6N	S940128_26N_10_Gilmore_1pt05inWP	Ti64	0.01	0.01	100	0.0020		10000000	2	1.1	high	variable		
Tistep block (TSB)	TSB_10f8_2pt6inWP	Ti64	0.01	0.01	100	0.0020	8	10000000	0.375	2.6	high			
Tistep block (TSB)	TSB_10f8_2pt6inWP_B	Ti64	0.01	0.01	100	0.0020	8	10000000	0.375	2.6	high			
Tistep block (TSB)	TSB_10f8_2pt6inWP_C	Ti64	0.01	0.01	100	0.0020	8	10000000	0.375	2.6	high/medium			
Tistep block (TSB)	TSB_10f8_2pt6inWP_D	Ti64	0.01	0.01	100	0.0020	8	10000000	0.375	2.6	high/low			
Tistep block (TSB)	TSB_10f8_3inWP	Ti64	0.01	0.01	100	0.0020	8	10000000	0.375	3.0	high/low			
Tistep block (TSB)	TSB_10f8_3inWP_B	Ti64	0.01	0.01	100	0.0020	8	10000000	0.375	3.0	high/<low			
Tistep block (TSB)	TSB_10f8_2pt8inWP	Ti64	0.01	0.01	100	0.0020	8	10000000	0.375	2.8	high/low			
Tistep block (TSB)	TSB_10f8_2pt5inWP	Ti64	0.01	0.01	100	0.0020	8	10000000	0.375	2.5	high/low			
Tistep block (TSB)	TSB_10f8_pt5inWP	Ti64	0.01	0.01	100	0.0020	8	10000000	0.375	0.5	med/low			
Tistep block (TSB)	TSB_10f8_pt5inWP_B	Ti64	0.01	0.01	100	0.0020	8	10000000	0.375	0.5	med/low			
Tistep block (TSB)	TSB_10f8_pt5inWP_C	Ti64	0.01	0.01	100	0.0020	8	10000000	0.375	0.5	med/low			
Tistep block (TSB)	TSB_10f6_2inWP (mislabeled; 1in actual WP)	Ti64	0.01	0.01	100	0.0020	6	10000000	1	1.0	high/medium			
Tistep block (TSB)	TSB_10f6_2inWP_B (mislabeled; 1in actual WP)	Ti64	0.01	0.01	100	0.0020	6	10000000	1	1.0	high			
Tistep block (TSB)	TSB_10f6_1inWP_2degIncident	Ti64	0.01	0.01	100	0.0020	6	10000000	1	1.0	high			
Tistep block (TSB)	TSB_10f6_1inWP_2degIncident_B	Ti64	0.01	0.01	100	0.0020	6	10000000	1	1.0	high			
Tistep block (TSB)	TSB_10_Gilmore_1pt25inWP	Ti64	0.01	0.01	100	0.0020	6	10000000	2	1.3	high			
Tistep block (TSB)	TSB_10_Gilmore_1pt25inWP_B	Ti64	0.01	0.01	100	0.0020		10000000	2	1.3	medium/low			
Tistep block (TSB)	TSB_10_Gilmore_1pt05inWP	Ti64	0.01	0.01	100	0.0020		10000000	2	1.1	low			
Tistep block (TSB)	TSB_10_Gilmore_pt85inWP	Ti64	0.01	0.01	100	0.0020		10000000	2	1.1	high			
S950320-5.2N	S950320_52N_10f6_2inWP	Ti64	0.01	0.01	100	0.0020	6	10000000	1	2.0	high/medium			
S950320-5.2N	S950320_52N_10f6_1pt2inWP	Ti64	0.01	0.01	100	0.0020	6	10000000	1	1.2	high			
S950320-5.2N	S950320_52N_10f6_pt8inWP	Ti64	0.01	0.01	100	0.0020	6	10000000	1	0.8	high			
S950320-5.2N	S950320_52N_10f6_1pt6inWP	Ti64	0.01	0.01	100	0.0020	6	10000000	1	1.6	high			
S950320-5.2N	S950320_52N_10_Gilmore_1pt25inWP	Ti64	0.01	0.01	100	0.0020	2.625?	10000000	1	1.3	low	Uniform		
S950320-5.2N	S950320_52N_10_Gilmore_1pt6inWP	Ti64	0.01	0.01	100	0.0020	2.625?	10000000	1	1.6	n/a	Uniform		
S950320-5.2N	S950320_52N_10_Gilmore_1inWP	Ti64	0.01	0.01	100	0.0020	2.625?	10000000	1	1.0	medium	Uniform		
S950320-5.2N	S950320_52N_10_Gilmore_0pt6inWP	Ti64	0.01	0.01	100	0.0020	2.625?	10000000	1	0.6	high/medium	Uniform		
D950209_5.2N	D950209_59N_10f8_1inWP	Ti64	0.01	0.01	100	0.0020	8	10000000	1	1.0	high	Low, Uniform		
D950209_5.2N	D950209_59N_10f8_3inWP	Ti64	0.01	0.01	100	0.0020	8	10000000	1	3.0	saturated			
D950209_5.2N	D950209_59N_10f8_3inWP	Ti64	0.01	0.01	100	0.0020	8	10000000	1	3.0	high	low, uniform		
D950209_5.2N	D950209_59N_10_Gilmore_5inWP	Ti64	0.01	0.01	100	0.0020	2.625?	10000000	1	5.0	n/a	Medium		
D950209_5.2N	D950209_59N_10_Gilmore_4pt25inWP	Ti64	0.01	0.01	100	0.0020	2.625?	10000000	1	4.3		Medium		
D950209_5.2N	D950209_59N_10_Gilmore_2inWP	Ti64	0.01	0.01	100	0.0020	2.625?	10000000	1	2.0	Low	Medium/High		
D950209_5.2N	D950209_59N_10f8_2pt7inWP	Ti64	0.01	0.01	100	0.0020	8	10000000	1	2.7	high	low, uniform		
F950508-1.5S	F950508-15S_5F8_2pt7inWP_10deg	Ti17	0.01	0.01	100	0.0020	8	5000000	0.75	2.7	high	low,uniform		
F950508-1.5S	F950508-15S_5F8_2pt7inWP_10deg_B	Ti17	0.01	0.01	100	0.0020	8	5000000	0.75	2.7	high	low,uniform		
F950508-1.5S	F950508-15S_5F8_2pt7inWP_10deg_C	Ti17	0.01	0.01	100	0.0020	8	5000000	0.75	2.7	high	low,uniform		
F950508-1.5S	F950508-15S_5F8_2pt7inWP_10deg_D	Ti17	0.01	0.01	100	0.0020	8	5000000	0.75	2.7	high	low,uniform		
F950508-1.5S	F950508-15S_5F8_2pt7inWP_10deg_E	Ti17	0.01	0.01	100	0.0020	8	5000000	0.75	2.7	high	low,uniform		
F950508-1.5S	F950508-15S_5F8_1inWP_10deg	Ti17	0.01	0.01	100	0.0020	8	5000000	0.75	1.0	high	low,uniform		
AF1	BlockAF1_I3_1inWP	Ti	0.01	0.01	100	0.0020	8	10000000	0.375	1.0				
AF1	BlockAF1_I3_pt5inWP	Ti	0.01	0.01	100	0.0020	8	10000000	0.375	0.5				
AF1	BlockAF1_10f6_2inWP	Ti	0.01	0.01	100	0.0020	6	10000000	1	2.0	high			
AF1	BlockAF1_10f6_4inWP	Ti	0.01	0.01	100	0.0020	6	10000000	1	4.0	saturated			
AF1	BlockAF1_10f6_4inWP_B	Ti	0.01	0.01	100	0.0020	6	10000000	1	4.0	high FBH			
AF1	BlockAF1_10f6_3inWP	Ti	0.01	0.01	100	0.0020	6	10000000	1	3.0	low SNR FBH			
AF1	BlockAF1_10f6_3inWP_B	Ti	0.01	0.01	100	0.0020	6	10000000	1	3.0	low SNR FBH			
AF1	BlockAF1_10f6_2pt5inWP	Ti	0.01	0.01	100	0.0020	6	10000000	1	2.5	med SNR target			
AF082	BlockAF082_10f6_2inWP	Ni	0.01	0.01	100	0.0019	6	10000000	1	2.0	saturated			
AF082	BlockAF082_10f6_2inWP_B	Ni	0.01	0.01	100	0.0019	6	10000000	1	2.0	saturated	low, uniform		
AF082	BlockAF082_10f6_2inWP_C	Ni	0.01	0.01	100	0.0019	6	10000000	1	2.0	high	low, uniform		
AF083	BlockAF082_I3_pt5inWP	Ni	0.01	0.01	100	0.0019	8	10000000	0.375	0.5	high	low, uniform		
AF083	BlockAF082_I3_1inWP	Ni	0.01	0.01	100	0.0019	8	10000000	0.375	1.0	low to high	low/uniform		
AF083	BlockAF082_I3_2inWP	Ni	0.01	0.01	100	0.0019	8	10000000	0.375	2.0	high	low/uniform		
AF083	BlockAF082_I3_3inWP	Ni	0.01	0.01	100	0.0019	8	10000000	0.375	3.0	high	low/uniform		
AF3	BlockAF3_I3_2inWP	Ni	0.01	0.01	100	0.0019	8	10000000	0.375	2.0	medium/high	low/uniform		
AF3	BlockAF3_I3_1inWP	Ni	0.01	0.01	100	0.0019	8	10000000	0.375	1.0	low-saturated	low/uniform		
AF3	BlockAF3_I3_1inWP_B	Ni	0.01	0.01	100	0.0019	8	10000000	0.375	1.0	low-high	low/uniform		
AF3	BlockAF3_I3_2inWP_B	Ni	0.01	0.01	100	0.0019	8	10000000	0.375	2.0	medium-high	low/uniform		
AF3	BlockAF3_I3_3inWP_KL	Ni	0.01	0.01	100	0.0019	8	10000000	0.375	3.0	medium-high	low/uniform		
S940128-2.6N	S940128_26N_Benchmark_I3_3inWP	Ti	0.01	0.01	100	0.0020	8	10000000	0.375	3.0	low-medium	high		
S940128-2.6N	S940128_26N_Benchmark_10F6_2inWP	Ti	0.01	0.01	100	0.0020	8	10000000	0.75	2.0	low-high	low		
S940128-2.6N	S940128_26N_Benchmark_10F6_3inWP	Ti	0.01	0.01	100	0.0020	8	10000000	0.75	3.0	low-high	low		
S940128-2.6N	S940128_26N_Benchmark_10F6_4inWP	Ti	0.01	0.01	100	0.0020	8	10000000	0.75	4.0	low-medium	high		
S940128-2.6N	S940128_26N_Benchmark_10F6_4inWP_B	Ti	0.01	0.01	100	0.0020	8	10000000	0.75	4	low-medium	low		
SA950320-5.2N	SA950320_52N_Benchmark_10F8_4inWP	Ti	0.01	0.01	100	0.0020	8	10000000	0.75	4	low-medium	low		
SA950320-5.2N	SA950320_52N_Benchmark_10F8_3inWP	Ti	0.01	0.01	100	0.0020	8	10000000	0.75	3	medium-high	low		
SA950320-5.2N	SA950320_52N_Benchmark_10F8_2inWP	Ti	0.01	0.01	100	0.0020	8	10000000	0.75	2	medium-high	low		
SA950320-5.2N	SA950320_52N_Benchmark_I3_3inWP	Ti	0.01	0.01	100	0.0020	8	10000000	0.75	3.0	low	high		
SA950320-5.2N	SA950320_52N_Benchmark_10F8_2inWP_B	Ti	0.01	0.01	100	0.0020	8	10000000	0.75	2.0	low	low		
D950209-5.2N	D950209_52N_Benchmark_10F8_1inWP	Ti	0.01	0.01	100	0.0020	8	10000000	1	1.0	medium-high	low		
D950209-5.2N	D950209_52N_Benchmark_10F8_2inWP	Ti	0.01	0.01	100	0.0020	8	10000000	1	2.0	medium-high	low		
D950209-5.2N	D950209_52N_Benchmark_10F10_2inWP	Ti	0.01	0.01	100	0.0020	10	10000000	1	2.0	medium-high	low		
D950209-5.2N	D950209_52N_Benchmark_10F10_3inWP	Ti	0.01	0.01	100	0.0020	10	10000000	1	3.0	medium-high	low		
D950209-5.2N	D950209_52N_Benchmark_10F10_4inWP	Ti	0.01	0.01	100	0.0020	10	10000000	1	4.0	medium-high	low		
D950209-5.2N	D950209_52N_Benchmark_I7_6inWP	Ti	0.01	0.01	100	0.0020	8	5000000	1	6.0	medium-high	low		
D950209-5.2N	D950209_52N_Benchmark_I7_6inWP_B	Ti	0.01	0.01	100	0.0020	8	5000000	1	6.0	medium-high	low		
D950209-5.2N	D950209_52N_Benchmark_5F8_6inWP	Ti	0.01	0.01	100	0.0020	8	5000000	1	6.0	low-high	low		